Pluto Hop, Skip, and Jump

NIAC Phase I

Final Report

For the period 9 May 2017 – 9 February 2018

Global Aerospace Corporation

14 February 2018

Grant Numbers: NNX17AJ71G and 80NSSC18K0062

GAC Report: 510-AJ71G-001

Distribution A: *Distribution is Unlimited*

Executive Summary

This is the Final Report from Global Aerospace Corporation on this NIAC effort (Grant Nos.: NNX17AJ71G and 80NSSC18K0062) to develop the Pluto Hop, Skip, and Jump mission concept. We sought out to establish the feasibility of using a large inflatable drag device to decelerate and land on Pluto from interplanetary speed (~14 km/s) using only the Pluto atmosphere and just a few kilograms of propellant. The design and analysis efforts in Phase I indicated that this is feasible. Aerodynamic heating and loads were found to be orders of magnitude less than typical planetary entries due to the ultra-low ballistic coefficient craft and the low density and large scale height of the Pluto atmosphere. The deceleration system is capable of delivering a 200-kg lander-hopper to the surface or inserting an orbiter of a similar mass using aerocapture. Mission analysis work led to a reference mission with Earth launch in 2029, Jupiter assist in 2030, and Pluto arrival in 2040.

Global Aerospace Corporation and its research partner, ILC Dover, have documented in this report the results of the design and analytical modeling efforts during the contract period (9 May 2017 – 9 February 2018). Key accomplishments include:

- Refined atmospheric models using the most recent *New Horizons* measurements and established the system-level requirements for a reference mission design,
- Performed interplanetary trajectory analysis to select a reference launch and arrival condition and analyzed Pluto arrival approach conditions to enable a lander mission,
- Used planetary aeroassist simulations to study the Pluto entry environment conditions including convective heating, g-loads, dynamic pressures, and evaluated the effect of atmospheric variation on the decelerator performance,
- Performed approach and landing analysis to determine the possible Pluto landing site locations based on the arrival geometry, and also performed an aerocapture analysis to evaluative feasibility of orbit insertion,
- Performed static structural, dynamic aeroelastic, CFD aerothermodynamics, and thermal analysis leading to a conceptual decelerator design,
- Developed a feasible materials solution for the decelerator envelope using conventional materials and softgoods fabrication techniques, generated an envelope patterning design, developed a load-distribution scheme, and generated an envelope system mass breakdown,
- Designed a lander-hopper payload, selected science payload components, evaluated hop performance at the surface, and generated a mass breakdown,
- Developed the integrated system conceptual design and mass breakdown.

1 Table of Contents

Table of Figures

Table of Tables

2 Introduction

A low-cost, *New-Frontiers*-class Pluto lander or orbiter mission is possible with a launch in 2029, Jupiter gravity assist in 2030, and arrival at Pluto in 2040. The next opportunity for a similar mission will not be available until 2042 when Jupiter is again positioned for a gravity assist.

So how can we land on or orbit Pluto without many hundreds of millions of dollars in nuclear power sources, a next generation launch vehicle, or a massive propulsion system?

One way is to launch a probe on a trajectory similar to *New Horizons* and on the approach trajectory deploy a large, lightweight inflatable drag device. The low density Pluto atmosphere has a scale height of ~60 km, nearly 8 times larger than at Earth, allowing the atmospheric drag to slowly dissipate the 50 gigajoules of kinetic energy from the incoming probe traveling at 14 km/s.

Contrary to prior thought, recent studies show that the Pluto atmosphere does not collapse and may have increasing atmospheric pressure with time in the current epoch [1], making the 2029 window attractive for this mission.

Only one nuclear power source, a Multi-Mission Radioisotope Thermoelectric Generator (RTG), which is currently in production by DOE, is needed to power onboard spacecraft systems. Depending on the trajectory and flight path angle, the probe can either descend to the surface and deliver a 200-kg lander-hopper or insert an orbiter via aerocapture. We deem this spacecraft and entry vehicle architecture *Entrycraft*.

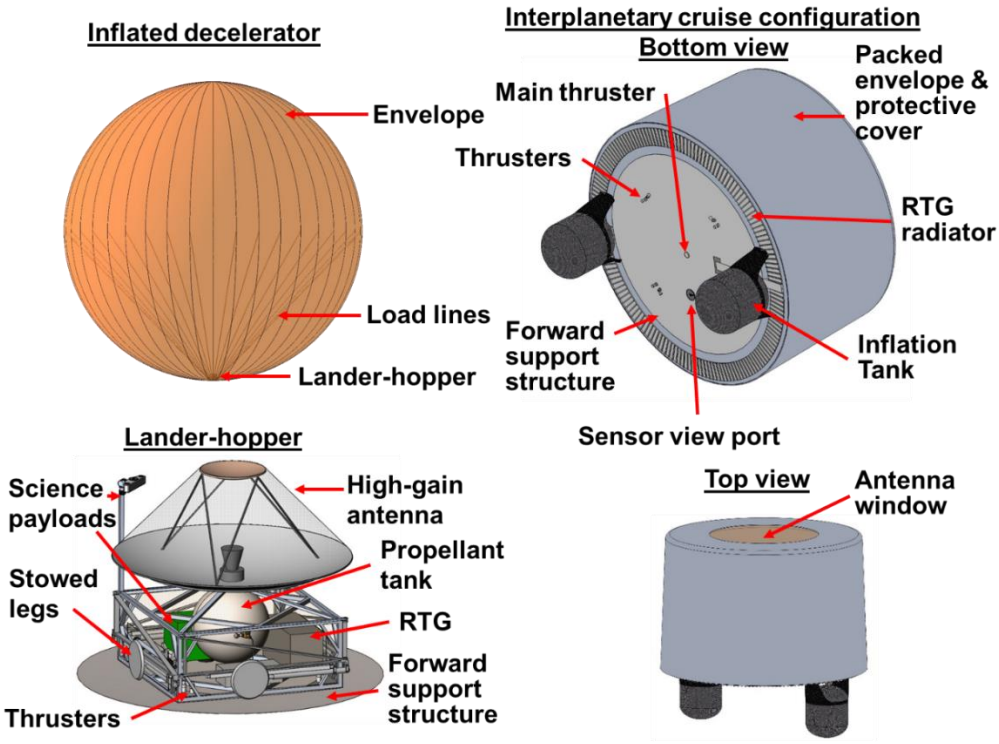

Figure 1. Entrycraft components (not to scale). Inflated envelope diameter is 70-m.

Upper-left: 70-m diameter inflated decelerator envelope with load lines, upper-right: interplanetary cruise configuration showing thrusters, RTG radiator, inflation tanks, and support structure, lower-left: lander-hopper showing science payload, antenna, propellant tanks, structure, and RTG, lower-right: top view of the stowed Entrycraft.

2.1 Innovation

This mission concept is enabled by the use of ultra-light-weight, Enveloping Aerodynamic Decelerator (EAD) technology* (Figure 1). The Entrycraft combines the decelerator system with the lander or orbiter payload that also performs all the needed function during the cruise to Pluto without a separate stage.

Why combine all systems into a single craft? Because the decelerator can enclose the lander within it during entry to protect it as it decelerates the system to terminal velocity. The non-rigid part of the decelerator is an inflatable thin film envelope that can be made extraordinarily large while remaining lightweight, reducing entry heating rates and dynamic pressures by orders of magnitude compared with current entry technology. Heat is radiated away through the film, on both the interior and exterior, eliminating the need for bulky and massive high-temperature thermal protection systems. The systems are also combined because the lander or orbiter can take advantage of the same systems as interplanetary cruise mode (communications, computer, attitude control, thrusters, power, etc.), and the rigid windward end of the decelerator can be used as the primary spacecraft support structure.

A roughly 330-kg, 70-meter diameter envelope and its load supporting elements can deliver a 200-kg probe to the Pluto surface or into orbit. For perspective, the envelope is smaller in diameter than the multi-ton scientific balloons NASA currently flies. Strong, lightweight load lines run from the payload to connection points at the envelope equator. The internal inflation pressure in the envelope opposes the compressive loads resulting from the deceleration forces during entry. This decelerator technology is easily transferrable to Entry, Deceleration and Landing (EDL) and aerocapture into orbit at other planetary bodies with both significant and tenuous atmospheres, including Earth, Mars, Venus, Titan, and Triton. The focus of this study is on a Pluto mission, particularly delivery of a Pluto lander to the surface though aerocapture was also studied to a limited extent.

The current near Pluto lander sequence is as follows:

(1) Deploy and inflate the decelerator envelope,

(2) Jettison the inflation tanks and cruise RTG heat exchanger,

(3) Enter the atmosphere at about 14 km/s with a nominal flight path angle of -63° at a reference altitude of 1600 km,

(4) Decelerate to a speed of about 80-100 m/s at several hundred meters above the surface,

(5) Separate the lander from the decelerator, deploy landing legs, and fire thrusters to land gently at the surface, making the propellant requirement for Pluto landing less than 8 kilograms,

(6) Perform science measurements at the initial landing site, and

(7) Fire the onboard thrusters to “hop” around the surface and investigate up to 10s of kilometers of distance.

This ConOps is illustrated in Figure 2.

* US Patent 9,884,693 issued February 6, 2018.

2.2 Science Application and Capabilities

The primary application for the Entrycraft is to deliver a lander-hopper to the surface of Pluto that has the ability to perform scientific investigations of the crust and atmosphere. These investigations could (1) shed new light on its origins and relationship to other Kuiper Belt objects and other planets using *in-situ* surface sampling and chemical analysis; (2) characterize the dynamics between the subsurface and the atmosphere by investigating outgassing processes such as cryovolcanism (hop over a plume!); (3) expand the understanding of surface geomorphology using hi-res imaging and IR spectrometry from multiple locations (on approach, during descent, and at the surface); (4) validate *New Horizons* measurements including atmospheric pressure and temperature profiles; (5) study the nature of the its crust and search for hypothesized [2] liquid water oceans using subsurface radar sounding, soil penetrometry, and perhaps a drill. In addition, the approach and descent imaging and measurements will be used to develop and plan the sequence of hops and jumps at the surface.

While the focus for this NIAC Phase I effort is a lander, another option for the Entrycraft is to insert a spacecraft into Pluto orbit via aerocapture. An orbiter could enable high-resolution image mapping of the entire surface, well beyond what *New Horizons* was able to capture. Furthermore, an orbiting spacecraft would also allow for detailed investigation of atmosphere composition and dust particles. The orbiter could also have the capability to release a small lander that could perform a short-duration surface science mission.

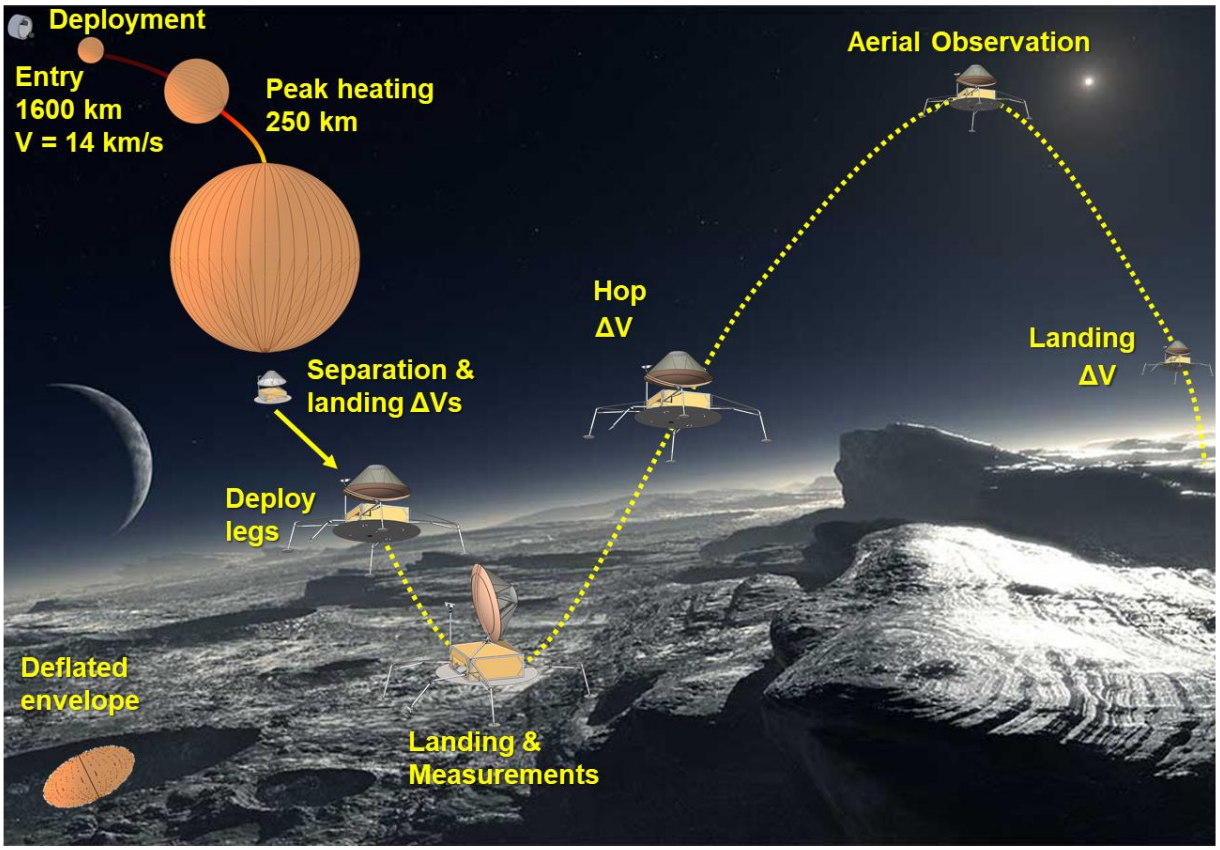

Figure 2. Concept of operations.

Entrycraft enters from interplanetary speed and deploys the envelope prior to entry. The decelerator reduces the speed to 100 m/s when the lander-hopper is released and performs a burn for landing. It subsequently uses its onboard propulsion system to explore the Pluto surface.

3 Phase I Project Tasks

In this section we summarize the Phase I project tasks that were carried out. We refined atmospheric models, system-level requirements, and concept of operations; evaluated entry trajectories; carried out the decelerator conceptual design and analysis; developed the lander-hopper conceptual design; and generated an integrated system mass breakdown.

3.1.1. Task 1: Refine Atmospheric Models, System-Level Requirements, and Concept of Operations

A detailed Pluto atmosphere model from *New Horizons* observations was compiled and integrated into a format for EDL analysis. Next, we established the system-level requirements. This began by generating a reference interplanetary trajectory from which the launch and arrival parameters could be established. We also selected a launch vehicle. We generated a notional payload design from which the lander design could be based. Finally, we considered an alternate Entrycraft ConOps for orbit insertion using aerocapture.

3.1.2. Task 2: Evaluate Entry Trajectories

In this second task, we used first-order planetary aeroassist simulations to characterize the Pluto entry environment including convective heating rates, dynamic pressures, and g-loads. We analyzed flight path angle time histories to assess skip-out and examined the effect of atmospheric variation on the decelerator performance. Next, we conducted an approach and landing analysis to determine the accessible landing sites given the Pluto orbit geometry and interplanetary velocity vector at time of arrival. Finally, we conducted an analysis to evaluate the feasibility of using EAD technology for orbit capture.

3.1.3. Task 3: Decelerator Design and Analysis

The majority of the work in this task focused on developing models and performing simulations to establish feasibility of the decelerator design concept. First, we performed structural analysis on the decelerator envelope to determine static stresses and deformations. This was used to establish the material requirements. Next we performed a low-order aeroelastic analysis to assess the susceptibility of the envelope to flutter during entry and descent. This was followed by an aerothermodynamics CFD analysis that was used to evaluate total heat flux including radiative heating from molecular dissociation and ionization in the shock layer. A thermal analysis that included internal convection was also used to determine component temperatures and evaluate inflation gas pressures during entry. Finally, the results from these data were used to develop a robust decelerator envelope design that could withstand the entry loads. This included materials selection, reinforcement design, envelope patterning, seam design, load distribution concept development, and generation of an envelope system mass breakdown.

3.1.4. Task 4: Lander-Hopper Conceptual Design

Since the primary technical innovation in this work is the entry system, we developed a conceptual-level design of the lander-hopper. We generated a lander-hopper design with CAD models and a component mass breakdown. We also computed hop trajectories and the propellant requirements.

3.1.5. Task 5: Conceptual Integrated System Design

In this final technical task, we compiled a list of components needed for the integrated Entrycraft during cruise to Pluto and generated a total launch mass breakdown.

3.1.1. Task 6: Planning and Reporting

We attended the NIAC orientation meeting on June 6-7, 2017, on September 21, 2018, we released a press release on the NIAC symposium briefing, presented the concept at the NIAC Symposium on September 25, 2017, submitted a Quarterly Report on December, 13, 2017, and submitted this Final Report on February 8, 2018.

4 Summary of Key Study Results

Below we summarize the key study results for this Phase I NIAC project:

- The Pluto atmosphere, based on *New Horizons* measurements, has sufficient density for deceleration by a large drag device at interplanetary speed, with a density from the surface to 400 km altitude that is roughly equivalent to the density at Earth from 70 to 120 km,
- The Pluto atmosphere does ***not*** freeze out and collapse as once thought,
- There is a *New-Horizons*-like interplanetary trajectory with a Jupiter assist available with launch in 2029 and Pluto arrival in 2040 (with Pluto arrival of ~14 km/s),
- Launch of the Entrycraft system can be done with the same vehicle used for *New Horizons*, i.e., the Altas 551 Star 48V launcher,
- The Entrycraft system has the ability to deliver a 200 kg lander-hopper to the surface or insert an orbiter of similar mass via aerocapture,
- The Pluto lander mission is enabled by one (1) Multi-Mission Radioisotope Thermoelectric Generator (MMRTG) providing 100 W of EOL power,
- First-order entry trajectory studies indicate convective heating rates and dynamic pressures that are on the order of 3 W/cm^2 and 30 Pa, respectively, several orders of magnitude less than heating and pressures seen during typical atmospheric entries from interplanetary speeds,
- The mild aeroheating environment during Pluto entry suggests the use of conventional, relatively low-temperature materials for the Entrycraft decelerator envelope, allowing it to have an ultra-low ballistic coefficient,
- Use of the decelerator is feasible at Pluto even with +/-50% variation in atmospheric density,
- Total entry masses of 400 – 700 kg are feasible for decelerator envelopes ranging from 70 to 80 meters in diameter,
- Approach and landing analysis indicated landing on the day side of Pluto is possible given the expected arrival geometry and several sites of interest in the Northern Hemisphere are accessible,
- Terminal velocity analysis showed that a delta-V of about 80 m/s is needed to slow the lander for landing, requiring approximately 7 kg of propellant,
- In an alternate ConOps for a Pluto orbiter, aerocapture is possible if the entry flight path angle is set to shallower angle than for direct entry, with one initial aerocapture orbit of 200 x 3000 km,
- Structural analysis using both analytical calculations and finite element analysis indicated peak envelope stresses of about 362 MPa and equatorial small deformations less than 20 cm,
- Structural analysis indicated that no additional envelope support elements are needed to maintain the spherical envelope shape during entry deceleration,
- Low-fidelity aeroelastic analysis suggests that flutter is unlikely as long as the inflation pressure is greater than the dynamic pressure by a small factor,

- Aerothermodynamics CFD analysis indicated minimal radiative heating during Pluto entry and a total heat flux that is just slightly higher than first-order model predictions, with a peak heat flux of about 3.5 W/cm^2,
- Thermal analysis, including internal inflation gas convection inside the envelope, showed envelope surfaces temperatures reaching about 520°C during peak heating and a peak gas temperature of 400°C,
- Low temperatures suggest that thermal protection materials are not required to enter the Pluto atmosphere from 14 km/s,
- An envelope materials study by our research partner, ILC Dover, indicated feasible material and seam designs that can be fabricated using existing materials and methodologies in the softgoods industry,
- Material fiber reinforcements can be used to increase envelope strength sufficiently to survive the deceleration loads at entry,
- The envelope system mass analysis resulted in an envelope minimum envelope mass of 337 kg, though a ~10% reduction is possible by reducing the amount of adhesive used in the system,
- The Entrycraft can deliver a lander-hopper to the surface of Pluto with the capability to use its onboard thruster system to travel a single horizontal distance of 50 km, though with smaller delta-Vs can make multiple hops of shorter distances
- A conceptual-level lander-hopper mass breakdown indicated a total CBE mass of 175 kg and a MEV mass of 214 kg
- A conceptual level integrated system mass breakdown indicated a CBE entry mass of 541 kg and an MEV entry mass of 639 kg, and a CBE launch mass of 726 kg and an MEV launch mass of 900 kg. This is below the launcher limit for the required C3 of about 1030 kg.

5 Refine Atmospheric Models, System-Level Requirements, and Concept of Operations

In this first task, we obtained and analyzed Pluto atmosphere data, identified system requirements from a reference interplanetary trajectory, developed a Pluto lander-hopper concept of operations (ConOps), and began analysis of an alternate, orbiter ConOps.

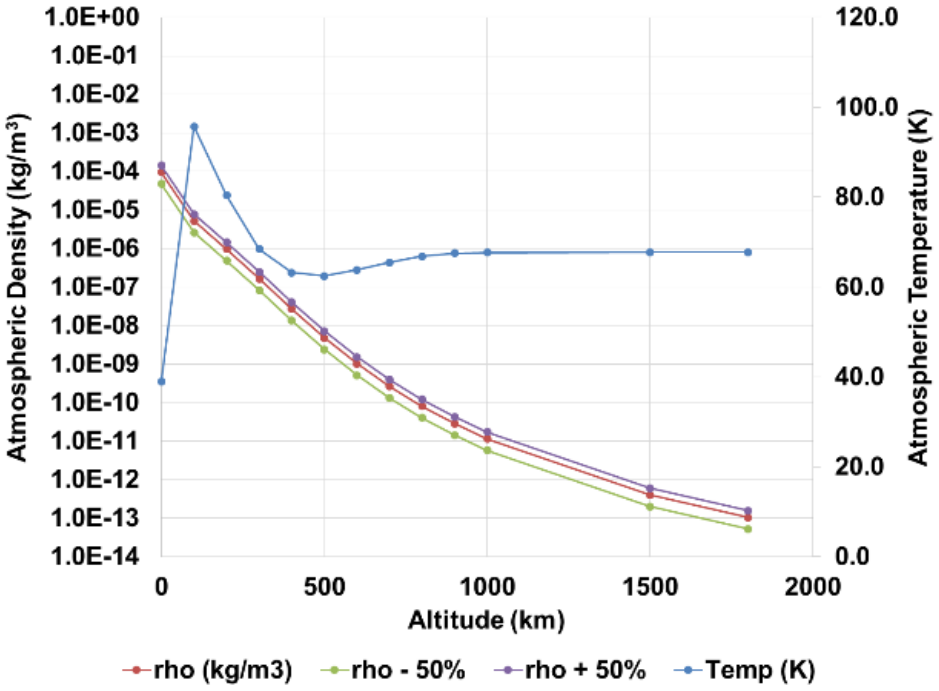

Figure 3. New Horizons Pluto atmosphere density and temperature profiles.

Atmospheric density ranges from order 10^{-4} kg/m^3 to order 10^{-13} kg/m^3 from the surface to 1500 km. Temperature at the surface is about 40 K and increases higher in altitude.

5.1 Atmospheric Modeling

A detailed Pluto atmosphere model from *New Horizons* observations was compiled and integrated into a format for EDL analysis. We obtained [3] the atmospheric pressure, number density, temperature, and species composition as a function of altitude. Figure 3 shows a subset of the processed data, particularly total density and temperature. The key parameter for determining the drag device feasibility at Pluto is the atmospheric density profile. The atmospheric density in the altitude range between the Pluto surface and 400 km is roughly equivalent in density to the 70 – 120 km altitude range on Earth, which we will later show to be ideal for the Entrycraft decelerator. Figure 3 also shows ± 50% density profiles that we will used to briefly assess effects of atmospheric measurement uncertainty.

5.2 System Requirements and Reference Interplanetary Trajectory

The next part of this task was to establish the system-level requirements. Key system-level requirements include launch energy; launch mass; flight time to Pluto, landed mass; power; landing site Earth communications and solar conditions; and lander duration of operation. A preliminary list of requirements is shown below.

- Launch Energy - <166 km^2/s^2
- Launch Mass <1030 kg
- Flight Time – <4400 days (12 years)
- Landed Mass – 200 kg
- Power – Less than or equal to 100 W or one MMRTG
- Earth Communications – Significant direct line-of-sight communications, e.g. >80% of time
- Solar conditions – Significant daylight conditions, e.g. >80% of time
- Lander duration of operation – >1 year
- Number of lander hops – two or more

In order to do determine if we could satisfy most of these requirements, we first analyzed several interplanetary launch windows for Earth to Pluto trajectories with a Jupiter gravity assist flyby. We then generated a reference interplanetary trajectory from which the launch requirements could be compared. We studied several launch opportunities and selected the 2028-2029 window for further analysis using a point-to-point conic (PPC) method. Because PPC analysis does not account for the gravity of any body besides the Sun, the approach velocity at Pluto was adjusted in accordance with a comparison of the PPC and actual trajectories for the New Horizons (NH) mission.

The primary difference between the PPC and the actual NH trajectory is the effect of Jupiter's gravity on the interplanetary trajectory. Compared to the PPC analysis, the actual NH trajectory flies by Jupiter 10 days later than, arrives at Pluto about 9 months later, and with an arrival speed about 1.5 km/s slower. Hence, we adjusted the PPC arrival speed by this amount. We decided not to change the arrival date for our analysis of arrival conditions since 9 months difference changes planetary and arrival geometry conditions by less than a degree (Pluto's position relative to the Sun changes by about 0.5°). In Phase II, we intend to re-analyze the interplanetary trajectory and make appropriate updates to account for a more accurate trajectory model. Note that we expect the launch C3 to be lower for this mission as compared to New Horizons, which means a somewhat larger launch mass could be assumed.

Figure 4 shows the Earth launch C3†, Pluto arrival velocity, and time of flight as a function of Earth launch date. Our reference trajectory has the following parameters: C3 of 116.64 km^2/s^2, Pluto hyperbolic approach speed of about 14 km/s, total time of flight of 11 years 8 months, Earth launch date of January 4, 2029, Jupiter assist date of July 2, 2030, Pluto arrival date of September 11, 2040. The Jupiter gravity assist requires a flyby at 3.6 Jupiter radii. Figure 5 shows the position of the planets at the Pluto arrival time.

Note, for reference the New Horizons trajectory parameters are shown including the launch C3 and equivalent Pluto hyperbolic approach speed (V-Infinity) as determined from PCC analysis.

Using the C3 from this reference trajectory, we determined the launch requirements. We assumed the same launch vehicle that was used for the New Horizons probe, i.e., the Atlas 551 Star 48 V IOS, though it is unlikely that exact launcher would be available in 2029. The allowable launch mass for our reference launch energy is 1030 kg. This vehicle's payload fairing diameter is nominally 3.75-m and the cylinder height is 4.2-m. This is more than sufficient to accommodate our baseline Entrycraft with required cruise components. The payload (lander or orbiter) mass is

† Hyperbolic escape energy per kg in units of km^2/s^2

therefore not limited by the launch vehicle in this case, but rather the entry loading limitations of the decelerator envelope. The decelerator envelope size, mass and lander-hopper mass, however, are limited by the launcher payload limits. Figure 6 shows the range of acceptable envelope sizes and the effect on the current best estimate (CBE) launch and system mass. Allowable envelope diameters are 70-100-m assuming an 8 μm film envelope with structural supporting elements and a lander or orbiter payload of 200 kg.

There were no other imposed requirements on the system by NASA or other sources. A science payload definition was not yet available from the science community so we generated a baseline suite of instruments with a current best estimate mass of 27.7 kg.

Table 1. Comparison of New Horizons Actual and PPC Trajectory with Pluto Hop, Skip and Jump PPC Trajectory.

Parameter	*New Horizons* Trajectory	*New Horizons* PPC Trajectory	Pluto Hop, Skip and Jump PPC Trajectory
Earth Launch Date	January 19, 2006	January 20, 2006	January 4, 2029
Launch C3	166.0	166.0	116.64
Jupiter Flyby Date	February 28, 2007	February 18, 2007	July 2, 2030
Jupiter Flyby Radius, R_J	32.25	27.3	3.63
Jupiter V-infinity, km/s	21.2	19.1	11.84
Pluto Arrival Date	July 14, 2015	October 23, 2014	September 11, 2040
Pluto V-infinity, km/s	13.7	15.15	15.12‡

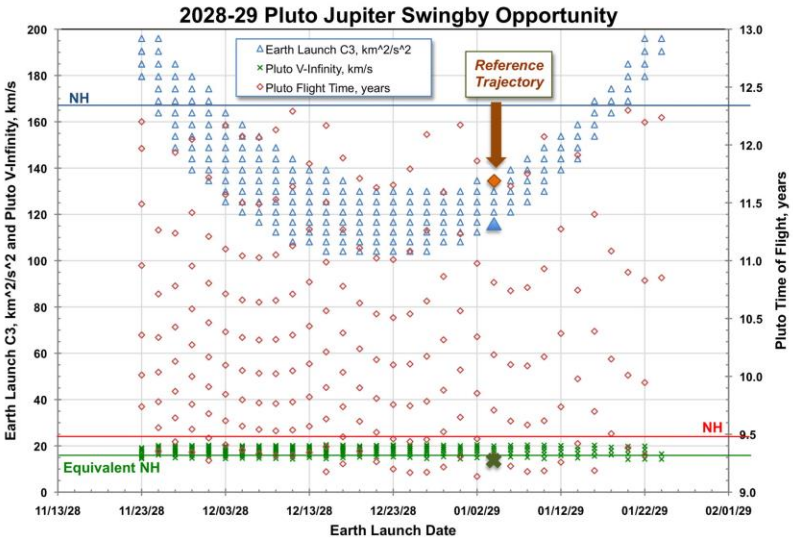

Figure 4. 2028-2029 Pluto mission parameter options.

Several possible trajectories are shown with different Earth launch dates, C3, Pluto arrival speed, and Pluto time of flight. A January 2029 reference trajectory is indicated.

‡ Based on *New Horizons* PPC trajectory result, equivalent entry speed of Pluto Hop, Skip, and Jump is approximately 14 km/s

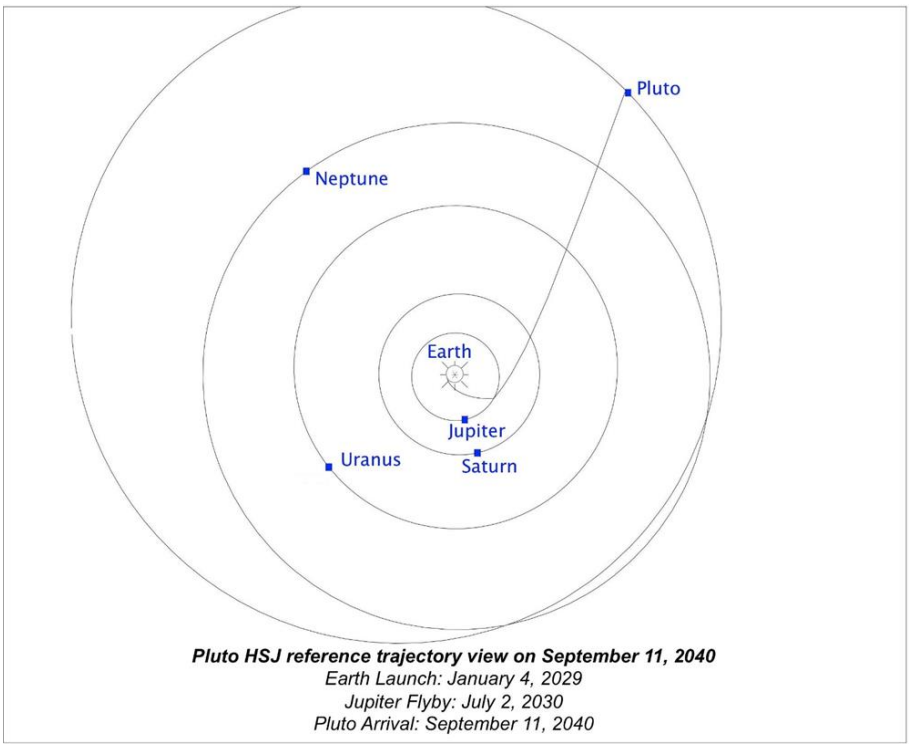

Figure 5. Position of the planets for the reference trajectory at Pluto arrival.

The trajectory from Earth to Pluto is shown in the ecliptic plane. The Jupiter gravity assist curves the flight path which remains straight until Pluto arrival.

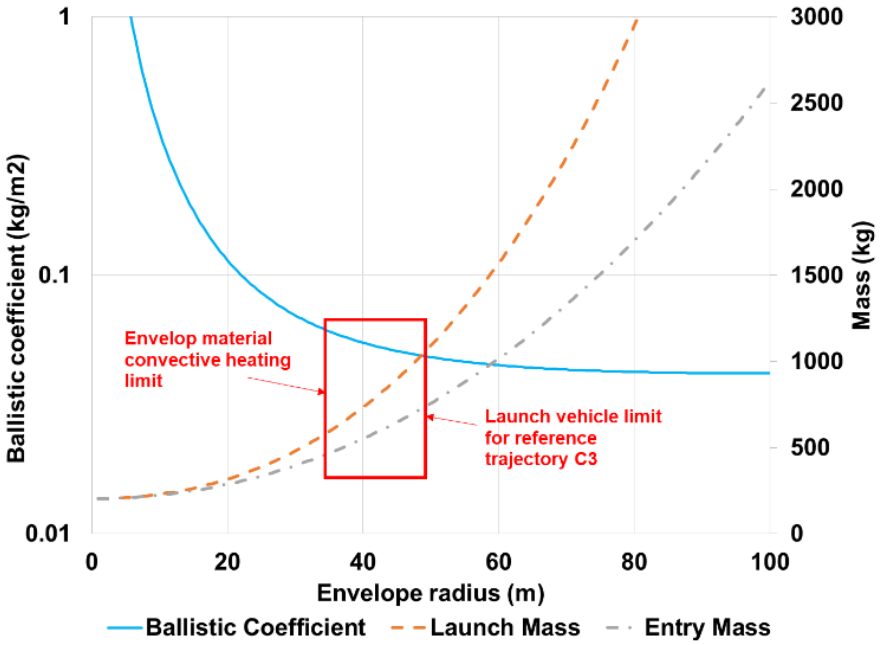

Figure 6. Effect of envelope size on ballistic coefficient and CBE launch and entry mass.

For relevant envelope sizes ranging in diameter from 70 to 100 m, the ballistic coefficient ranges from 0.068 to 0.055, the launch mass ranges from 625 to 1030 kg, and the entry mass ranges from 500 to 880 kg.

5.3 Concept of Operations

The launch of the Pluto Hop, Skip and Jump mission is assumed in early January of 2029 on board a launcher with upper stage that can achieve the boost to high hyperbolic escape speed. At injection, the Entrycraft is spin stabilized to enable the use of a simple solid rocket motor escape stage. After injection, the spin rate is reduced to about 3-5 rpm for the duration of cruise. The Earth escape velocity at infinity will be about 10.8 km/s, corresponding to a C3 of 116 km^2/s^2 that will carry the Entrycraft to a Jupiter in about a year and a half. At least two trajectory correction maneuvers (TCMs) will be carried out between Earth and Jupiter; one shortly after launch and another on the approach to Jupiter.

Flyby of Jupiter in July of 2030 requires a close approach of 3.6 Jupiter radii of the planet or about 188,000 km from the top of its atmosphere and inside Io's orbit. For this close approach to Jupiter, particle radiation will be significant requiring protection in the form of radiation hard electronics and shielding. Fortunately, the flyby is fast keeping the total dose lower than NASA's Juno spacecraft, now orbiting Jupiter.

During cruise the Entrycraft will periodically re-orient its spin axis and the high gain antenna towards Earth for periodic communications and navigation radiometric data. After Jupiter flyby, there will be at least two planned TCMs; one to correct the flyby errors at Jupiter and the last to adjust the approach trajectory for the proper flight path angle and timing for entry. After Jupiter, except for TCMs, the Entrycraft goes into a quiescent phase to reduce Entrycraft operations until near Pluto approach about 10 years later. Prior to approach, the Entrycraft begins final navigation operations that could include optical images of Pluto and its star background by means of an optical navigation camera located behind a protective glass window on the forward support structure pointing approximately 180° to the direction of the high-gain antenna. This optical navigation activity, combined with Earth-based radio navigation and a final TCM, will reduce the approach targeting errors, facilitate achieving the proper Pluto entry flight path angle, and adjust the timing to ensure landing at a desired site on Pluto that was selected based on the *New Horizons* data.

Prior to entry, the Earth communications are transferred to the low-gain antenna and attitude orientation thrusters precess the Entrycraft's spin axis into the entry orientation. At this point the decelerator envelope is deployed and inflated with helium gas. Deployment and inflation, which will significantly reduce the spin rate, could occur several minutes to several hours before entry after which the inflation tanks are jettisoned. Pluto entry interface occurs at a range of about 1600 km from the surface of Pluto about 15-20 minutes before landing. At this point the flight path angle target is -63° to ensure entry heating and deceleration loading does not exceed the material limits of the envelope. During entry and landing, the optical navigation camera images the Pluto surface at an increasingly higher resolution. These images will be used for subsequent planning for hopping operations. For a 70-m diameter envelope and a flight path angle of -63°, peak stagnation point heating rate, dynamic pressure and g-load of 3.4 W/cm^2, 32 Pa, and 30 gees occur a little over 2 minutes into the entry sequence. Most of the entry sequence time is spent at an altitude below 100 km at a terminal velocity below about 125 m/s. Upon reaching ~700 m above the surface, the lander separates from the envelope and performs a translation maneuver to avoid the slowed, but still descending, envelope and then the lander executes a propulsive burn to land on the surface of Pluto.

Once on the surface, the high-gain antenna is deployed and begins a search maneuver in the direction of the sun for a radio signal from Earth. After signal acquisition, entry and landing data

can be communicated to Earth. Following lander-hopper systems checkout, science operations commence with imaging, surface sampling and soil mass spectrometry, geophysical sounding, heat flow and seismometry, as well as atmospheric sampling.

Once, the initial landing site science objectives are completed, a hop to another landing site is planned based on a combination of *New Horizons* data and the optical navigation camera images taken on entry. A small propulsive burn is executed to put the lander on a parabolic trajectory toward a second landing site. During the hop, imaging and spectroscopy data of the surface will be obtained. A final propulsive burn is preformed just prior to touchdown for landing.

6 Evaluate Entry Trajectories

This task involved three primary subtasks: (1) Lander entry trajectory parameter studies, (2) Pluto approach and landing analysis, and (3) Aerocapture analysis.

6.1 Entry Trajectory Parameter Studies.

The lander entry trajectory parameters studies were conducted using GAC's Hypersonic Planetary Aeroassist Simulation System (HyperPASS) trajectory analysis tool [4]. HyperPASS enables users to perform guided aerocapture, guided ballute aerocapture, aerobraking, orbit decay, or unguided entry simulations at any of seven target bodies (Venus, Earth, Mars, Jupiter, Titan, Neptune, or Pluto). Pluto was added to the software for this NIAC effort and the most recent New Horizon's Pluto atmosphere data (Figure 3) was used. HyperPASS has been validated using NASA's Program to Optimize Simulated Trajectories (POST), a 3 degree of freedom entry analysis system. HyperPASS has been used by GAC for NASA aeroassist and launch approval studies and for US Army missile trajectory studies.

The purpose of the Phase I effort was to determine a set of feasible working parameters for the decelerator and entry trajectory that could deliver the lander-hopper to the surface. To do this we computed entry convective stagnation point heating rates, g-loads, dynamic pressures, and altitude and flight path angle time histories. HyperPASS computes convective heating rates based on the Sutton-Graves approximation:

$$q_{conv} = Cv^3\sqrt{\frac{\rho}{R_n}} \qquad (1)$$

Where v is the velocity, ρ is the atmospheric density, R_n is the vehicle nose radius, and C is a convective heating coefficient that depends on the atmospheric composition. HyperPASS does not compute radiative heating but this analyzed separated using CFD and presented in Section 7.3.

Four envelope diameters were considered: 70-m, 80-m, 90-m, and 100-m. We computed trajectories for entry flight path angles (FPA) ranging from -59 to -65 degrees. Total entry masses ranged from 450 to 750 kg and were based on a 200 kg lander payload plus the appropriately-scaled decelerator envelope CBE mass based on envelope component mass estimates. The Pluto arrival speed was fixed at 14 km/s based on the reference mission design.

We began by examining the altitude time history as a function of flight path angle and envelope diameter. This analysis was used to determine the conditions in which atmospheric skip-out is likely. Figure 7 shows that skip-out occurs for all envelope sizes when the entry FPA is -59 degrees or greater. Skip-out also occurs for the 70-m envelope at an entry FPA of -60 degrees. In all cases, an entry FPA of -61 degrees or less appears to prevent skip-out. However, analysis of FPA time histories is necessary to ensure the FPA remains negative during the entire trajectory. A change in sign of the FPA from negative to positive could also indicate susceptibility to skip-out if there are small changes in atmospheric density. Figure 8 shows the FPA time histories for the four envelope diameters. We see that an initial FPA of -60 is insufficient because the FPA temporarily becomes positive later in the trajectory. In a real mission scenario, it will be necessary to obtain an updated atmosphere profile from Earth-based stellar occultation analysis and/or a precursor probe in order to determine the entry FPA. A precursor probe, if needed, would be a small, battery-powered, instrumented sphere that would be released from the entrycraft a few weeks prior to arrival and

placed on a Pluto intercept trajectory. Upon entry, it would transmit data to the Entrycraft for relay to Earth. For the 2040 arrival, we expect the atmosphere to have remained nearly the same or increased in density based on recent simulations [1]. Next we calculated convective stagnation point heating rates, dynamic pressure, and g-load time histories. The results are given in Figure 9, Figure 10, and Figure 11, respectively. In this design space, peak convective heating rates range from 1.7-3.2 W/cm^2, peak dynamic pressures range from 15-42 Pa, and peak g-load ranges from 16-36 g depending on the entry FPA and envelope size. The g-loading is not very sensitive to envelope diameter tends to increase very slightly with increasing size. However, g-loading is very sensitive to entry FPA and increases with steeper angles. Both heating rates and dynamic pressures decrease with increasing envelope diameter and shallower FPAs.

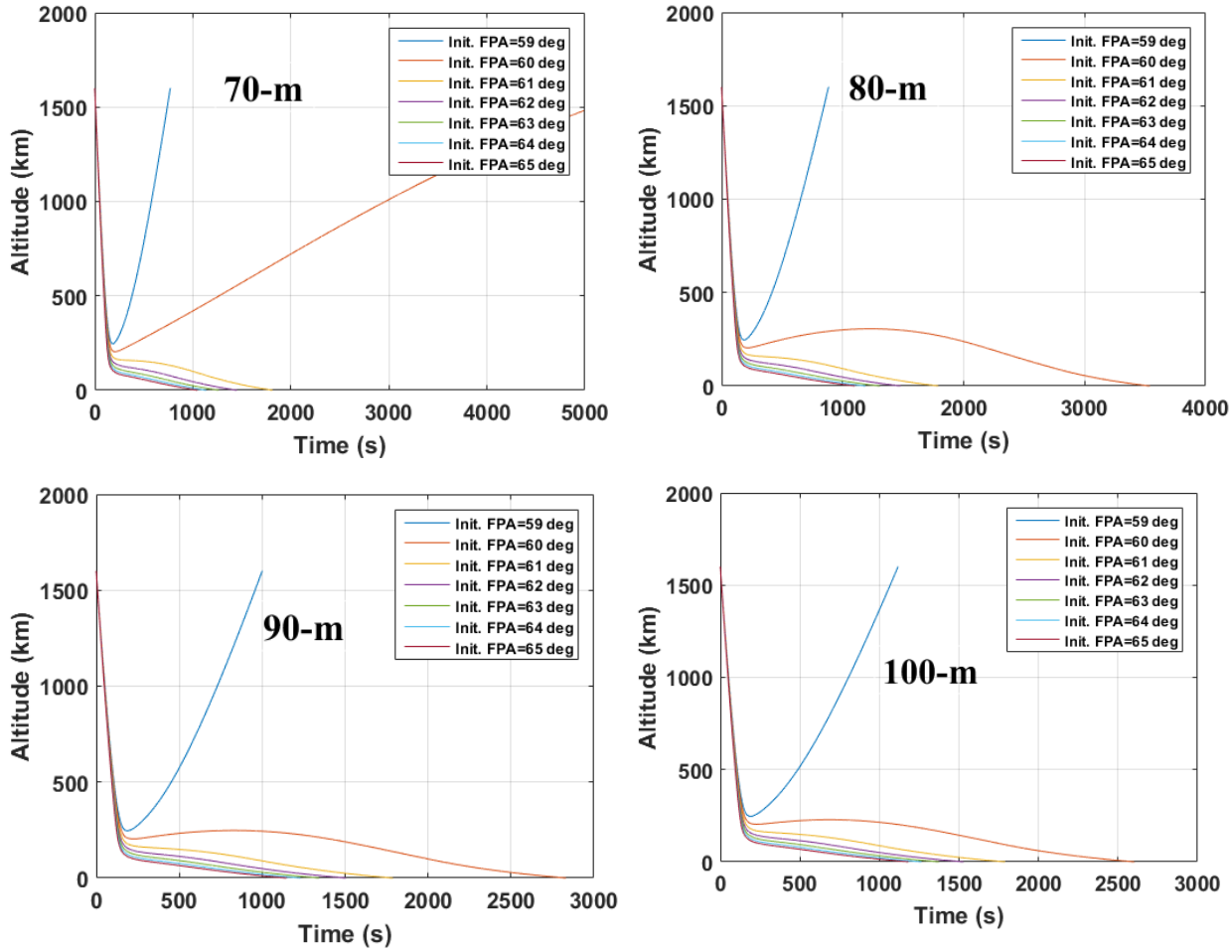

Figure 7. Entrycraft altitude time histories for several entry FPAs and envelope diameters.

Upper-left: altitude time history for the 70-m diameter envelope, indicating skipout for an entry flight path angle of -60°, upper-right, altitude time history for the 80-m diameter envelope, indicating skipout for an entry flight path angle of -59°, lower-left, altitude time history for the 90-m diameter envelope, indicating skipout for an entry flight path angle of -59°, lower-right, altitude time history for the 100-m diameter envelope, indicating skipout for an entry flight path angle of -59°.

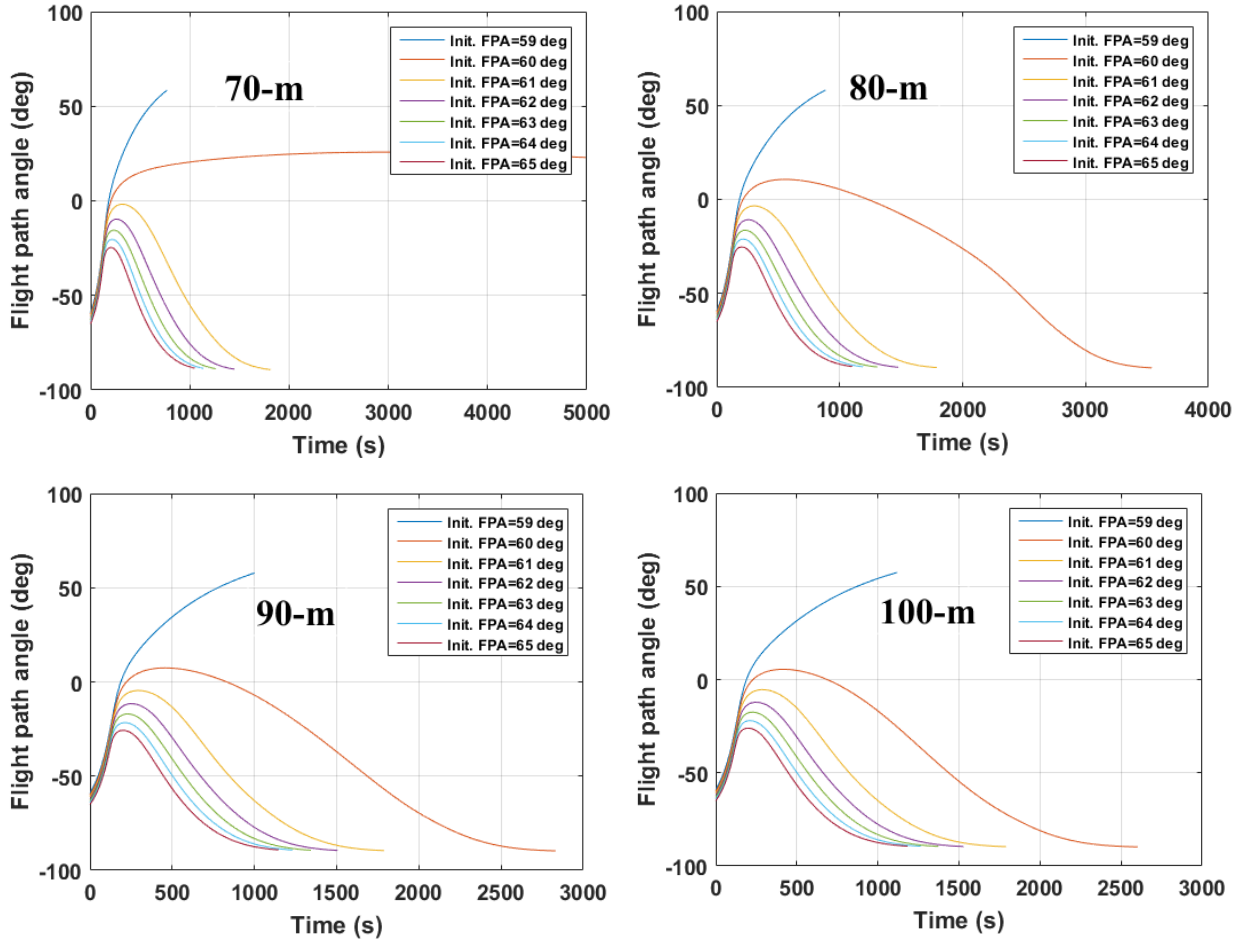

Figure 8. Entrycraft FPA time histories for several entry FPAs and envelope diameters.

Upper-left: flight path angle time history for the 70-m diameter envelope, indicating skipout for an entry flight path angle of -60°, upper-right, flight path angle time history for the 80-m diameter envelope, indicating skipout for an entry flight path angle of -59°, lower-left, flight path angle time history for the 90-m diameter envelope, indicating skipout for an entry flight path angle of -59°, lower-right, flight path angle time history for the 100-m diameter envelope, indicating skipout for an entry flight path angle of -59°. Curves indicate that transition to positive flight path angles during entry indicate susceptibility to skipout.

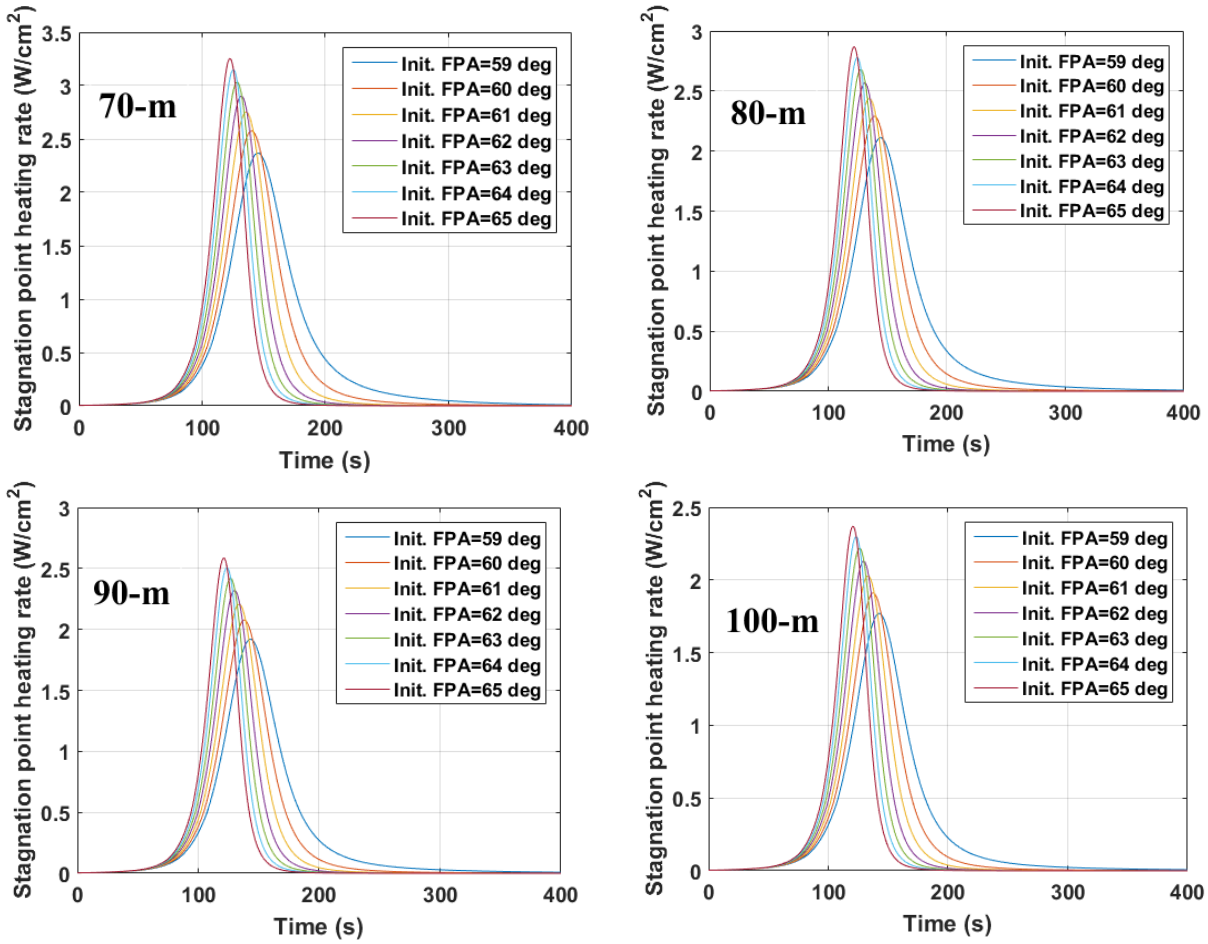

Figure 9. Entrycraft convective stagnation point heating time histories.

Upper-left: convective stagnation point heating time history for the 70-m diameter envelope, indicating peak heating range of 2.4 -3.25 W/cm^2 for entry flight path angles ranging from -59° to -65°, Upper-right: convective stagnation point heating time history for the 80-m diameter envelope, indicating peak heating range of 2.1 -2.8 W/cm^2 for entry flight path angles ranging from -59° to -65°, Lower-left: convective stagnation point heating time history for the 90-m diameter envelope, indicating peak heating range of 1.9 -2.55 W/cm^2 for entry flight path angles ranging from -59° to -65°, lower-right: convective stagnation point heating time history for the 100-m diameter envelope, indicating peak heating range of 1.75 -2.4 W/cm^2 for entry flight path angles ranging from -59° to -65°.

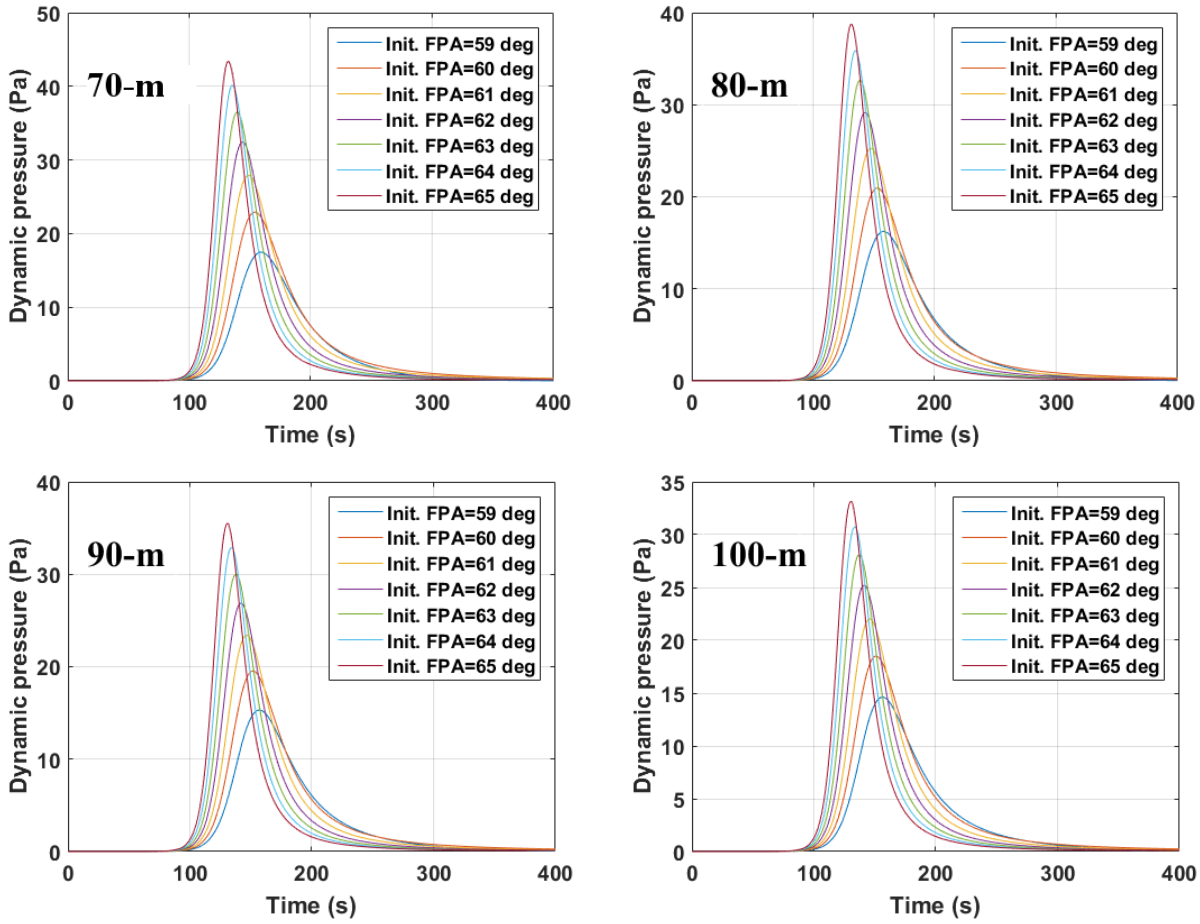

Figure 10. Entrycraft dynamic pressure time histories.

Upper-left: dynamic pressure time history for the 70-m diameter envelope, indicating peak dynamic pressure range of 17 – 42 Pa for entry flight path angles ranging from -59° to -65°, Upper-right: dynamic pressure time history for the 80-m diameter envelope, indicating peak dynamic pressure range of 16– 39 Pa for entry flight path angles ranging from -59° to -65°, lower-left: dynamic pressure time history for the 90-m diameter envelope, indicating peak dynamic pressure range of 15 – 35 Pa for entry flight path angles ranging from -59° to -65°, lower-right: dynamic pressure time history for the 100-m diameter envelope, indicating peak dynamic pressure range of 15 – 33 Pa for entry flight path angles ranging from -59° to -65°.

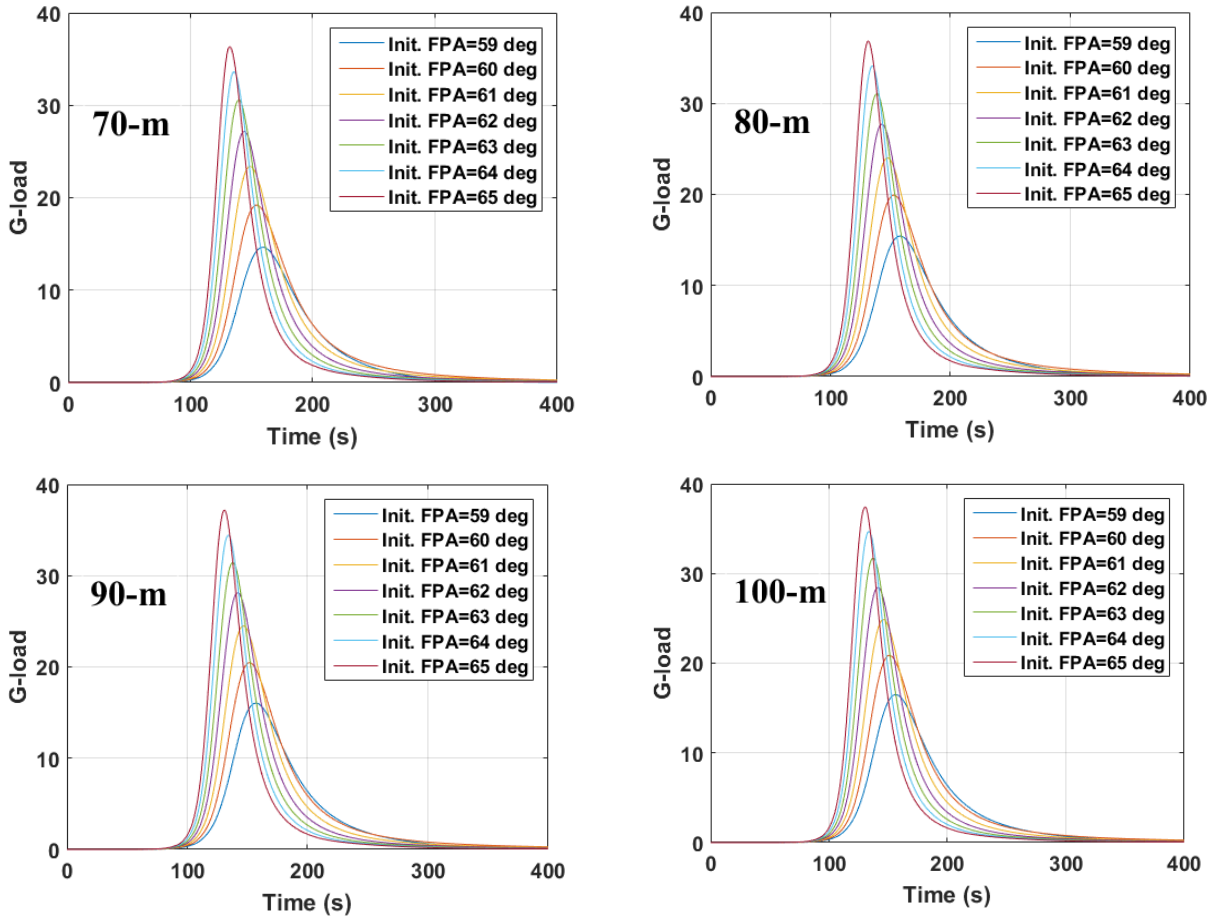

Figure 11. Entrycraft g-load time histories.

Upper-left: g-load time history for the 70-m diameter envelope, indicating peak g range of 14 – 36 g for entry flight path angles ranging from -59° to -65°, Upper-right: g-load time history for the 80-m diameter envelope, indicating peak g range of 15 – 36 g for entry flight path angles ranging from -59° to -65°, lower-left: g-load time history for the 90-m diameter envelope, indicating peak g range of 16 – 37 g for entry flight path angles ranging from -59° to -65°, lower-right: g-load time history for the 100-m diameter envelope, indicating peak g range of 16.5 – 37 g for entry flight path angles ranging from -59° to -65°.

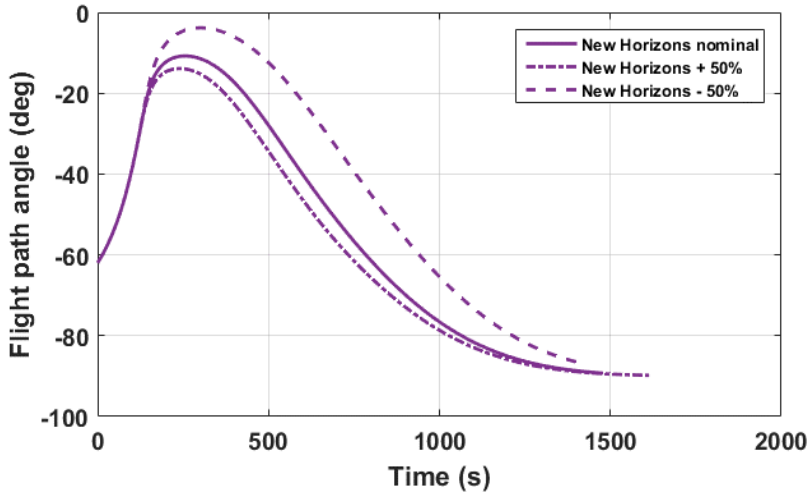

Figure 12. Effect of atmospheric variation on the entry FPA time history. Entry FPA=-62°.

The effect of increasing the nominal New Horizons atmosphere density by 50% is small and tends to keep the flight path angle slightly steeper during entry. Decreasing the nominal density by 50% causes a more significant shallowing of the flight path but skipout does not occur.

The entry system favors shallower entry FPAs from a g-load and heating perspective, but this increases the risk of skip-out. Based on these data and the convective heating limits of the envelope material, we believe the acceptable range of entry FPAs are -61° to -64° with the current *New Horizons* atmosphere. The nominal entry FPA should be -62° or -63° depending on the envelope size. B-plane analysis using the acceptable range of entry FPAs indicates the maximum B-plane target error is about 175 km. This is commensurate with the 184 km B-plane target error that was seen for *New Horizons* 14 Days prior to arrival. Since *New Horizons* showed that trajectory control and targeting at Pluto can be done successfully, it is likely that these errors can be reduced even further for our proposed mission in 2029.

Next, we analyzed the effect of atmospheric variability on the entry trajectories. We started with the *New Horizons* density profile and generated new profiles that were increased and decreased by a factor of 50% over all altitudes. We feel this is a very generous bound for the density variation based on past measurements and predictions of Pluto atmospheric variation [6]. The effect of atmospheric variability on the FPA time history for an entry FPA of -62° is given in Figure 12. We observe the decrease in density by 50% causes a noticeable decrease in the FPA later in the trajectory but it remains negative at all times, i.e. does not approach skipout. G-loading is reduced by 10% and heating rates decrease by 4%. An increase in density appears to have a less noticeable effect. In this case g-loading increases by 6% and heating rates increase by 2.6%. While it does not appear that atmospheric density variation is a major driver of the system design, the atmosphere should be sampled remotely, at least by Earth-based star occultations, a few weeks before entry such that the entry FPA can be updated if necessary.

Next we down-selected the envelope diameter. A clear comparison of the effect of diameter on convective heating and dynamic pressure is shown in Figure 13. The heating rates and dynamic pressures are relatively low throughout the range of diameters. Heating is consistently below the high-temperature, operating limits of the envelope materials under consideration. Dynamic pressures range from 25-32 Pa and are easily managed by inflating the envelope with a greater internal pressure. These results seem to suggest that there is no significant system-design benefit

of having an envelope larger than 70 meters in diameter. Also, larger envelopes will increase launch mass and inflation system weight. There is a small benefit to going to 80 meters with regard to skipout since the ballistic coefficient is smaller and there is more flexibility. We will consider both 70-m and 80-m cases in our later analysis efforts.

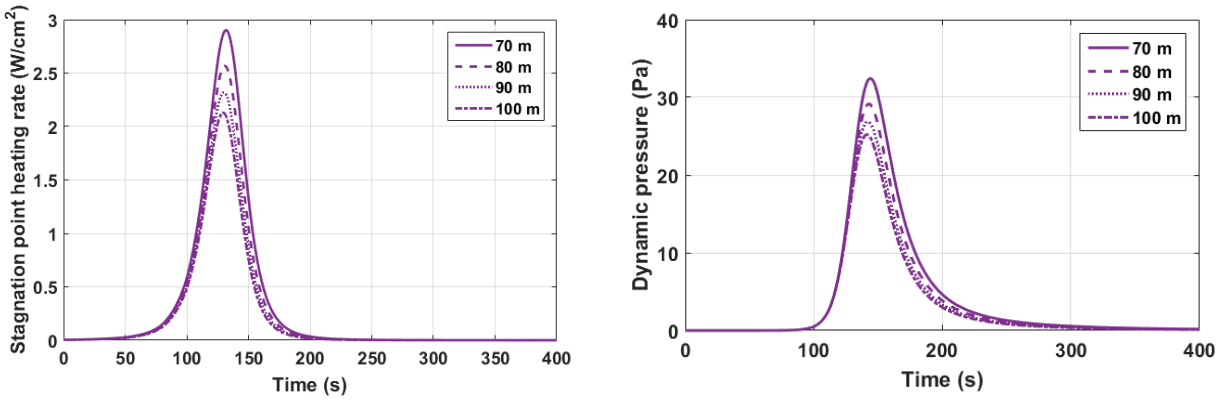

Figure 13. Effect of envelope diameter on stagnation point heating and dynamic pressure. FPA=-62°.

Top: Stagnation point heating time histories for envelope diameters of 70-100 m, bottom, dynamic pressure time histories.

Finally, we evaluated the effect of entry mass on heating rates for fixed envelope sizes. In the previous analyses, we scaled the entry mass based on the envelope size, and the mass for a given envelope size was fixed. Here, we look at varying that mass. Figure 14 shows the effect of entry mass on the convective stagnation point heating for the 80-m envelope and an entry FPA of -62°. Varying the mass from 400 to 700 kg results in a change in heating from 2.36 to 3 W/cm^2. Results for the 70-m envelope and an entry FPA of -63° are shown in Figure 15. Varying the mass by the same amount results in a change in heating from 2.9 to 3.8 W/cm^2. This indicates that a large change in entry mass has a relatively small effect on heating and provides greater flexibility in the design.

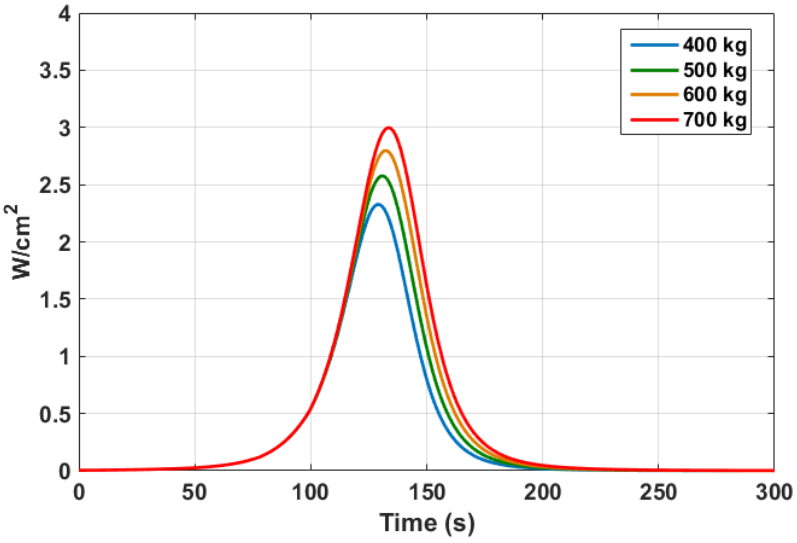

Figure 14. Effect of total entry mass on the convective stagnation point heating for the 80-m diameter envelope, entry FPA=-62°.

Stagnation point heating rates range from about 2.36 to 3 W/cm^2 for entry masses of 400 to 700 kg, respectively.

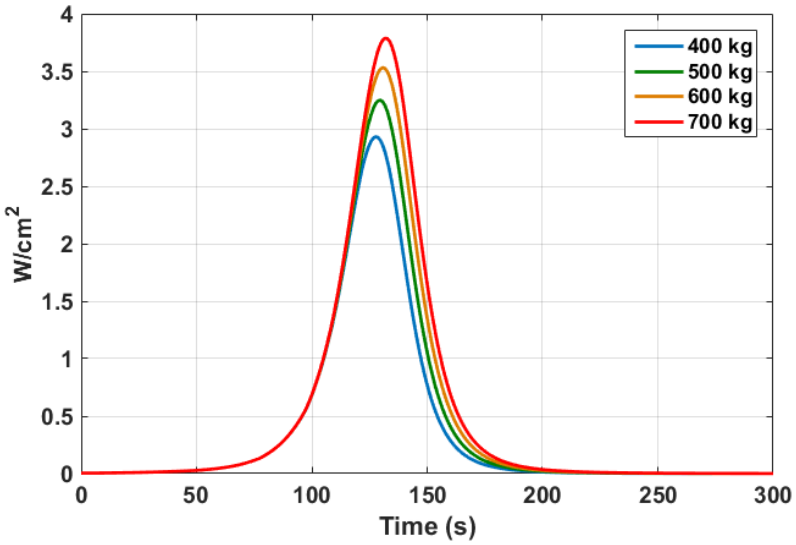

Figure 15. Effect of total entry mass on the convective stagnation point heating for the 70-m diameter envelope, entry FPA=-63°.

Stagnation point heating rates range from about 2.9 to 3.8 W/cm^2 for entry masses of 400 to 700 kg, respectively.

6.2 Approach and Landing Analysis.

After establishing feasibility of the decelerator for use at Pluto, we carried at an approach and landing analysis to determine if placing a lander on the dayside of Pluto was possible given the entry flight path angle constraints. We generated the reference approach and landing geometry in the V-infinity-sun plane using the position of Pluto in orbit at the arrival time. This is shown in Figure 16. Here we used the 80-m diameter envelope (the 70-m diameter envelope will have a narrower entry corridor). The Earth-Sun terminator divides the dayside and night side, and we desire to place a lander on the dayside for continuous communications with Earth. The green shaded region indicates the potential landing area and the green lines indicate the landing area on the dayside. The flight path angle range allows us a ~375 km landing region on the dayside. The effect of atmospheric uncertainty on the landing footprint is an aspect that requires further study. While we've shown that relatively large (±50%) changes in atmospheric density are not problematic for decelerator feasibility at Pluto, an updated density profile at time of arrival is desirable to targeting the optimal entry flight path angle. Stellar occultations or a precursor probe would be able to provide this data. A Monte Carlo analysis is needed to evaluate quantitatively the effects of these and other uncertainties on the landing footprint.

Regarding stellar occultations, the first confirmed detection of Pluto's atmosphere was by Ellliot in 1993 [5] [6] [7]. We expect that a concerted international effort similar to that occurred two weeks prior to *New Horizons* flyby would make observations of the atmosphere of Pluto prior to an aerocapture mission to confirm atmospheric density prior to arrival. The *New Horizons* effort found that Pluto's atmosphere was still expanding, with a significant pressure increase of about 5% since 2013 and a factor of almost three since 1988. They found that this trend ruled out an atmospheric collapse associated with Pluto's recession from the Sun, at least for the New Horizon's mission [8]. Earth-based stellar occultations would be a necessary aspect of this mission to provide final targeting information. An orthographic view on approach at the reference mission arrival time is shown in Figure 17. We can access several surface features of interest in the

Northern hemisphere depending on the timing of arrival. An example landing site and its path in the Pluto day is also indicated.

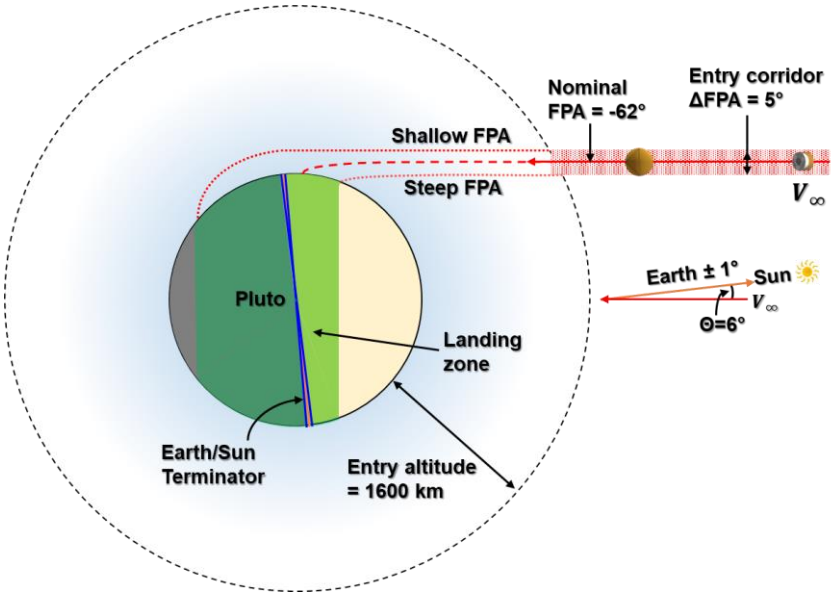

Figure 16. Pluto reference approach and landing region. Envelope diameter is 80-m in this analysis.

This figure shows the reference approach and landing geometry in the V-infinity-sun plane. The Earth-sun terminator divides the day side and night side. The angle between the Sun and V-infinity vector is about 6°. The nominal FPA is -62° and an entry corridor width is 5 degrees. The day-side landing zone is about 375-km long in this entry scenario. The shallower flight path angles tend towards landing on the night side.

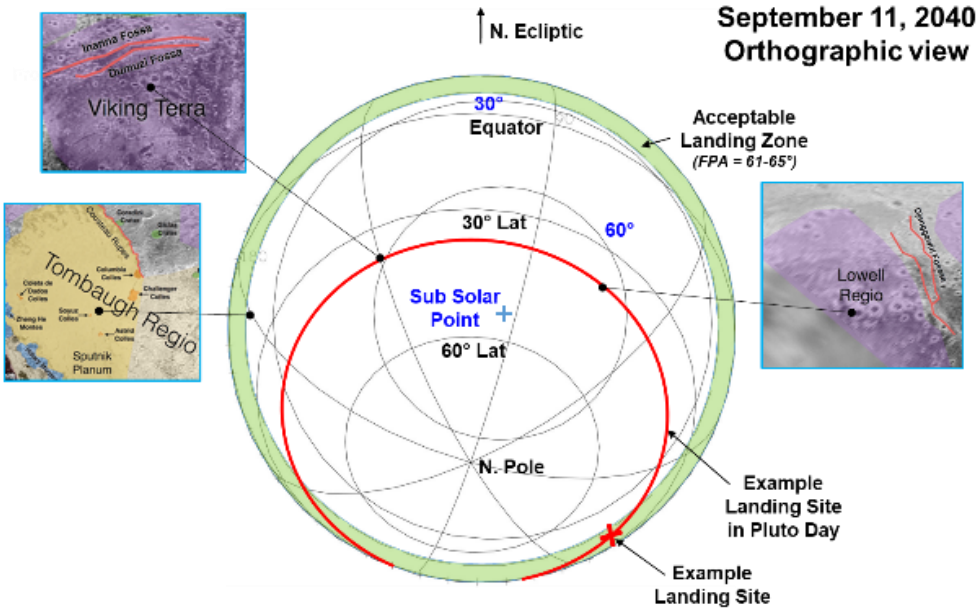

Figure 17. View on approach to Pluto.

This view on approach for the reference trajectory shows several possible landing sites that are accessible including the Viking Terra, Tombaugh Regio, and Lowell Regio. The subsolar point is indicated at 53.5 deg latitude and the North Pole and Equator are also shown. The acceptable landing zone is indicated by a region of linear distance along the edge of the Pluto surface. As Pluto rotates, different landing sites become accessible. An example landing site is shown at about 35 degrees latitude.

6.2.1. Terminal Velocity Analysis

Next we computed the terminal velocity of the decelerator before lander separation and used that to determine the propellant mass required for landing. These parameters are heavily dependent on the drag coefficient. In this Reynolds number regime, the drag coefficients range from 0.1 to 0.5 depending on the surface roughness. Any roughness of the decelerator skin or seams is very small with respect to the diameter so we assume the surface to be smooth. This results in a drag coefficient of 0.5. The terminal velocity is about 80 m/s and the required propellant mass (assuming monopropellant with I_{sp}=240s) is 7 kg. We will include substantial margin to assure enough propellant is available for a safe landing

6.3 Aerocapture Analysis.

While the primary focus of our study is on a decelerator for EDL and delivery of a lander to the surface, significant science interest in a Pluto orbiter led us to study briefly the feasibility of aerocapture at Pluto. We used HyperPASS to generate aerocapture trajectories using the existing spherical decelerator design. With an initial flight path angle of -59.8° and the same entry speed of 14 km/s, we can enter into an initial aerocapture orbit of 200 x 3000 km and then perform a burn to raise periapsis to 1600 km. This is illustrated in Figure 18. Heating rates and dynamic pressures are slightly less than for EDL because the entry angle is shallower. The velocity time history and atmospheric effects on flight path angle are shown in Figure 19. We see that aerocapture is possible even when the atmosphere is 50% greater or less dense than recent *New Horizons* measurements. The required entry flight path angles for the nominal atmosphere, ±0%, +50%, and -50% density are -59.23°, -59.32°, and -60.8°, respectively. Since the decelerator does not have lift, the atmospheric characteristics must be known accurately at time of arrival. For an orbiter, a precursor probe or extensive Earth-based (and possibly space-based) stellar occultations could be used to obtain an atmospheric update, and thrust maneuvers may be used to account for other off-nominal effects.

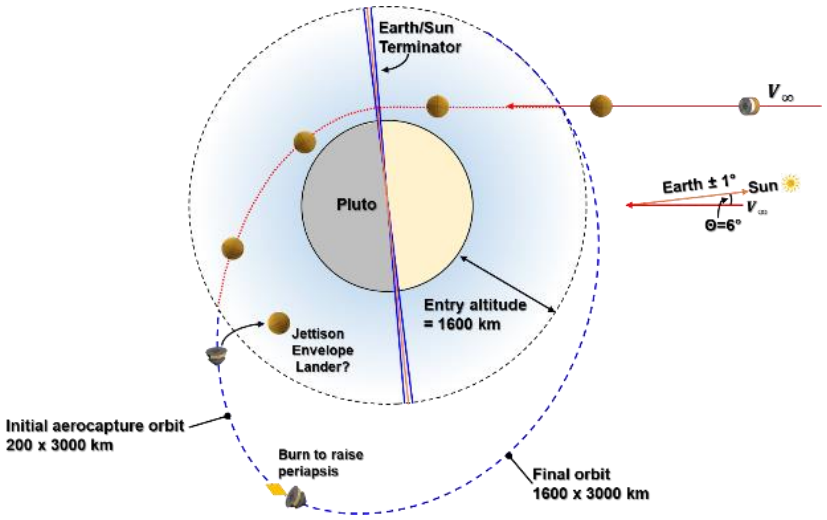

Figure 18. Aerocapture mission option using Entrycraft. Entry FPA = -59.8°.

The Entrycraft enters at a precise flight path angle and passes through the Pluto atmosphere after which the envelope is jettisoned. An initial aerocapture orbit of 200 x 3000 km is shown. We indicate a burn to raise

In addition, a ConOps could include post close approach, adaptive EAD envelope release based on integrated acceleration measurements to obtain a precise final orbit. Other options could include the use of small propulsive delta-Vs to shape the final orbit during the atmospheric pass.

This is a subject for further study.

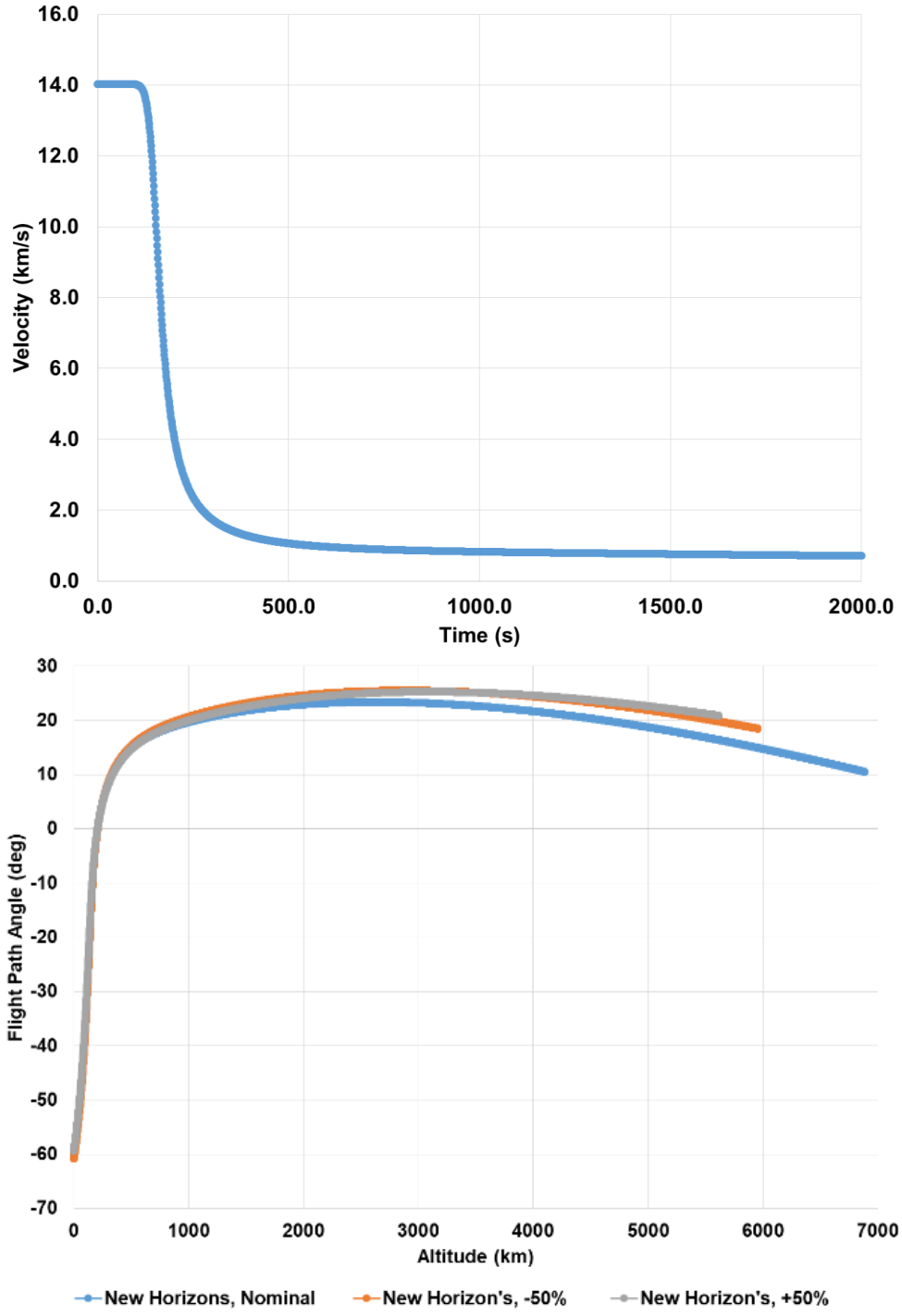

Figure 19. Aerocapture velocity profile (top) and effect of atmosphere variability on flight path angle (bottom).

The aerocapture velocity time history shows the velocity decreasing from 14 km/s to about 700 m/s after the pass through the atmosphere. The effect of atmospheric variability is to shift slightly the required entry flight path angle needed to attain orbit capture.

7 Decelerator Design and Analysis

In this task, we developed models of the decelerator envelope in order to establish key design requirements. Structural analysis was performed to determine the required envelope strength. Aeroelastic analysis was used to assess flutter instabilities. Aerothermodynamics CFD analysis was used to evaluate radiative heating effects and verify the HyperPASS predictions of convective heating. A thermal model was also developed to determine more accuracy the surface and inflation gas temperatures. Finally, this analysis was used to develop a decelerator envelope materials design and fabrication approach, and an envelope patterning design.

7.1 Structural Modeling

The two primary objectives of this modeling were to 1) calculate the stress field in the envelope material to establish material strength requirements and 2) determine if any additional high-pressure inflatable structures would necessary to prevent excessive inward deformation at the load line attachment points at the envelope equator. We carried out a structural stress and deformation analysis using simple calculations and FEA simulations.

7.1.1. Structural Model Assumptions

The assumptions used in this analysis are as follows:

- Uniform envelope material, seams neglected (a seam design and analysis is provided in the Appendix
- Uniform line loads at the envelope equator (neglects load line attachment points)
- Thermal effects on material properties neglected
- Payload-envelope attachment point neglected
- 80-m diameter envelope is considered (this is conservative due since stress ~ radius)
- Envelope film thickness of 70 μm (2.75 mil)

7.1.2. Structural Model

The maximum stress in the envelope can be estimated using the following equation:

$$\sigma = \frac{pr}{2h} + \frac{F_z}{h} \qquad (2)$$

where the first term is the stress due to internal pressure in a spherical shell and the second term is the stress due to the payload weight distribution into the equator. The equivalent tangential line force per length, F_z, is computed by dividing the payload force during deceleration by the circumference of the envelope. Table 2 provides the magnitudes of the accelerations, forces and internal pressures assumed for this analysis.

Table 2. Parameters for the structural analysis. 80-m diameter envelope.

	Peak Heating	Peak G-load
Acceleration (a), m/s^2	187	271
Equivalent Radial line Force (F_r), N/m	105	153
Equivalent Tangential Line Force (F_z), N/m	105	153
Initial Internal Pressure (P_{int}), Pa	148	142

	Peak Heating	Peak G-load
Drag Force§ (D), N	92,890	134,800

The FEA model was set up according to the loads and displacements in Figure 20**.** This model is an approximation of the structure and does not include the payload and load lines, though it does include their representative forces. The model consists of a spherical envelope without a torus. The forces due to the load lines are represented by a radial line force (F_r) and tangential line force (F_z) per length applied at the equator as shown. An acceleration body force (a) is applied to the entire model. This corresponds to g-loading experienced during entry. Internal pressure from the gas (P_{int}) is applied and external static pressure is assumed to be zero. A drag force (D) corresponding to the peak dynamic pressure is applied on the windward surface of the envelope. A fixed-point boundary condition, constraining displacements in all three directions, is enforced at the stagnation point. The payload mass is distributed into the envelope as an increase in density which is sufficient for a static analysis.

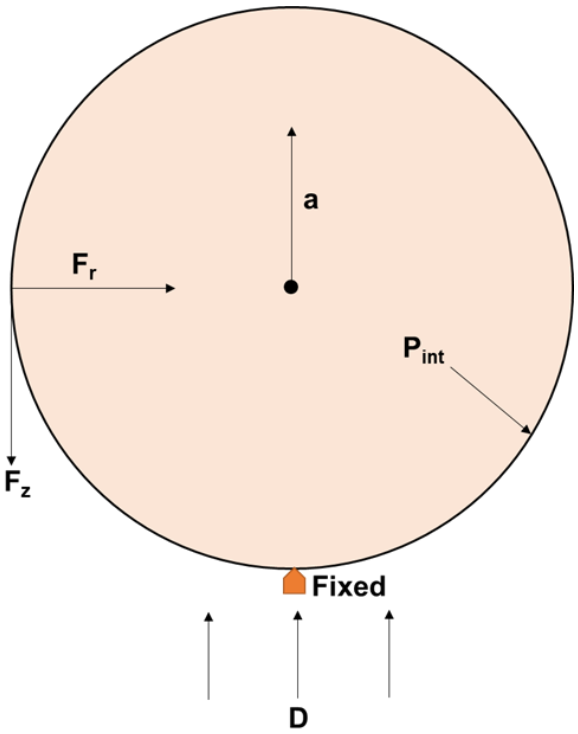

Figure 20. Loads and displacements for the FEA model.

A cross-section of the spherical envelope is shown with loads applied. There is a fixed constraint at the stagnation point, drag, acceleration, internal pressure, and radial and tangential line forces applied at the equator.

The envelope is meshed with triangular shell elements. The mesh density is increased at the equator where the payload forced are distributed. The higher mesh density in this region allows the expected inward deformation and complex stress field to be resolved more accurately.

7.1.3. Structural Model Results

Maximum Stress. Using the parameters in Table 2, we performed stress calculations and found the maximum stress at peak heating and peak g-load to be **362** and **353 MPa**, respectively. The stress is relatively constant between these two conditions for the following reasons. During peak heating the internal pressure is at a maximum and the g-loading is about 60% of maximum, but g-loading only accounts for 10-15% of the total envelope stress. During peak g-loading the internal pressure is reduced by 4% and the g-load is at a maximum. The two effects nearly cancel out and the envelope mechanical loading remains fairly constant during the two loading regimes.

Stress and Deformation Fields. In order to determine the stress field and deformations within the envelope, we initially performed a linear static analysis and determined that it was insufficient to resolve accurately the deformed shape of the envelope. We then switched to a nonlinear static analysis that accounts for large deformation effects. While this approach was able to resolve the

§ Drag coefficient is a function of Mach number and is equal to 0.9 during peak heating and peak dynamic pressure

static shape of the envelope, it would not converge due to an artifact of the FEA analysis when the envelope thicknesses was less than about 70 μm (2.75 mil). As a result we had to artificially increase the envelope thickness by about a factor of 8.33 (from 8.4 μm [0.33 mil] to 70 μm [2.75 mil]) while reducing the envelope material density accordingly. As a result of this artifice, the computed stresses needed to be scaled by the thickness change to reflect the actual stress in the thinner material. We will need to refine this analysis in a later effort to solve the thinner material configuration, but believe the current approach to be sufficient in this initial feasibility study.

After making this change to envelope thickness, we performed this nonlinear static analysis using the parameters in Table 2. We verified that all the forces balanced and the model remained constrained at the stagnation point during application of the loads. Application of the internal pressure (calculated in the thermal analysis) caused the envelope volume to increase slightly, which in turn decreased the pressure slightly. The final pressure used in the analysis was determined by iteration. Volume changes due to material stretching were on the order of 4% and the final pressures were found to be a few Pascals lower than the initial pressures. For example, the initial and final pressures for the peak heating case were 148 and 142 Pa, respectively.

The FEA solutions for the peak heating and peak g-loading cases are provided in Figure 21. The true scale radial deformations indicate that the forces applied at the equator do not result in very large inward deformations. The maximum equatorial (inward) deformation for the 70 μm (2.75 mil), 80 meter envelope is about 10 cm for peak heating and about 18 cm for the peak g-load cases. This deformation does not change significantly with thickness, so we expect it to be similar in magnitude for the 8.4 μm [0.33 mil] envelope. These relatively small deformations suggest that additional inflatable structural elements, like an internal toroid, as originally proposed, are not needed, but additional structural modeling should be performed.

In Figure 21 we present the deformation and stress results on 1X and 50X scaled meshes. **The 50X scale exaggerates the overall combined effect of the loads.**

Next we calculated the equivalent (Von Mises) stress. Von Mises stress is typically compared to the yield strength of the material for safety factor calculations. The maximum equivalent stress of the 70 μm (2.75 mil) envelope during peak heating and peak g-loading is 41.1 and 39.3 MPa, respectively. Assuming linearity in thickness the equivalent stresses of the 8.4 μm (0.33 mil) envelope are 349 and 334 MPa, respectively.

Principal stresses were also calculated. The middle principal stress runs longitudinally and the maximum principal stress runs circumferentially along the envelope. The maximum principal stress of the 70 μm (2.75 mil) envelope during peak heating and peak g-loading is 42.9 and 42.1 MPa, respectively. Assuming linearity in thickness the equivalent stresses of the 8.4 μm (0.33 mil) envelope are 364.6 and 357 MPa, respectively. These results are comparable to the earlier hand calculations.

7.1.4. Structural Analysis Conclusions

In summary, the structural analysis indicates the following:

1. The peak heating condition results in slightly larger envelope stress than peak g-loading due to the greater internal pressure,
2. An inflatable structural element at the envelope equator is not needed since radial deformation due to distributed payload forces is less than 20 cm,

3. The Von Mises criterion indicates the envelope yield strength must be greater than 350 MPa. We suggest a 3X factor of safety for the envelope, for a yield stress of > 750 MPa.
4. Further work is needed in the FEA model development to allow simulation of the physical envelope thickness and incorporate features such as the payload load line load distribution patches.

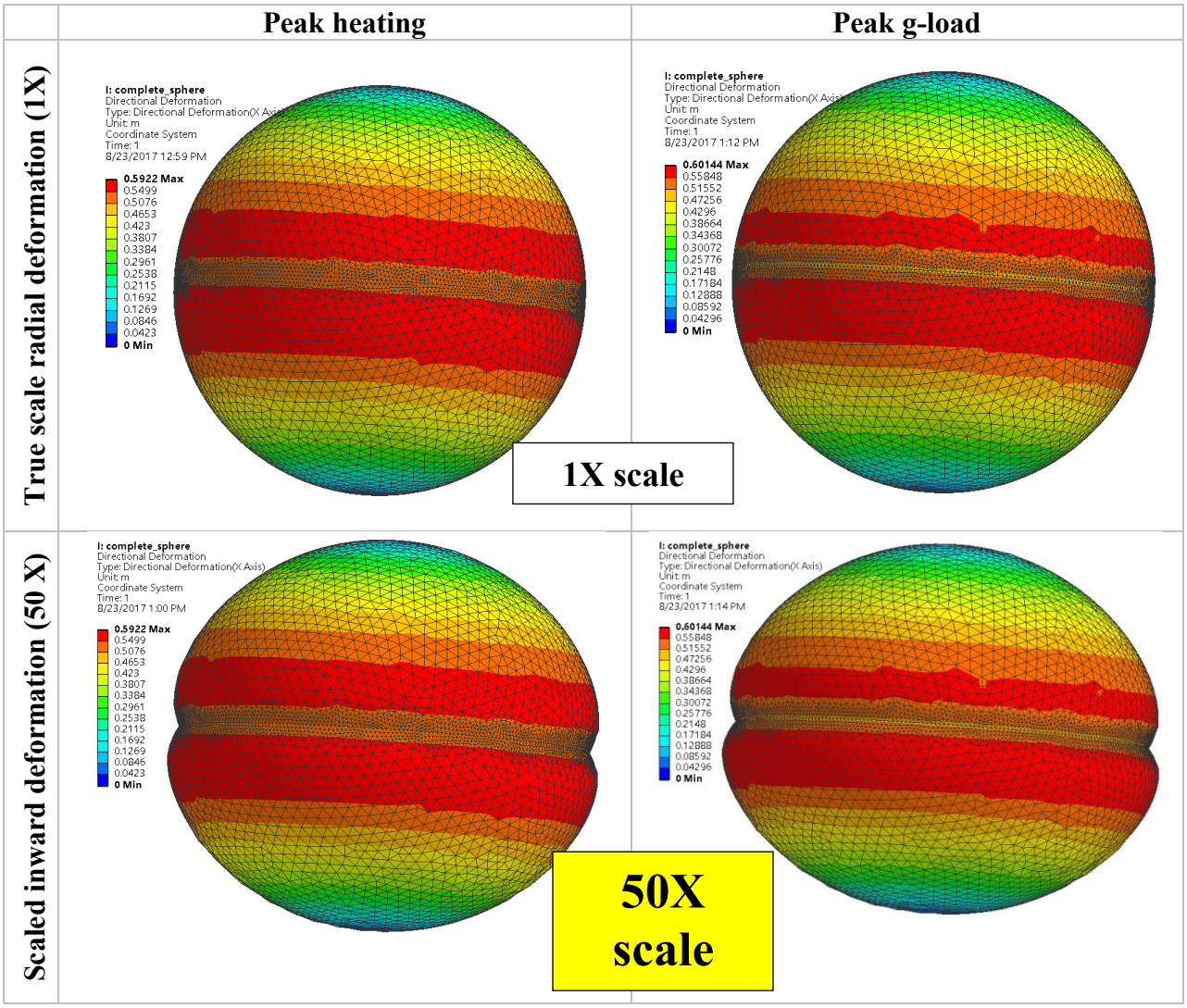

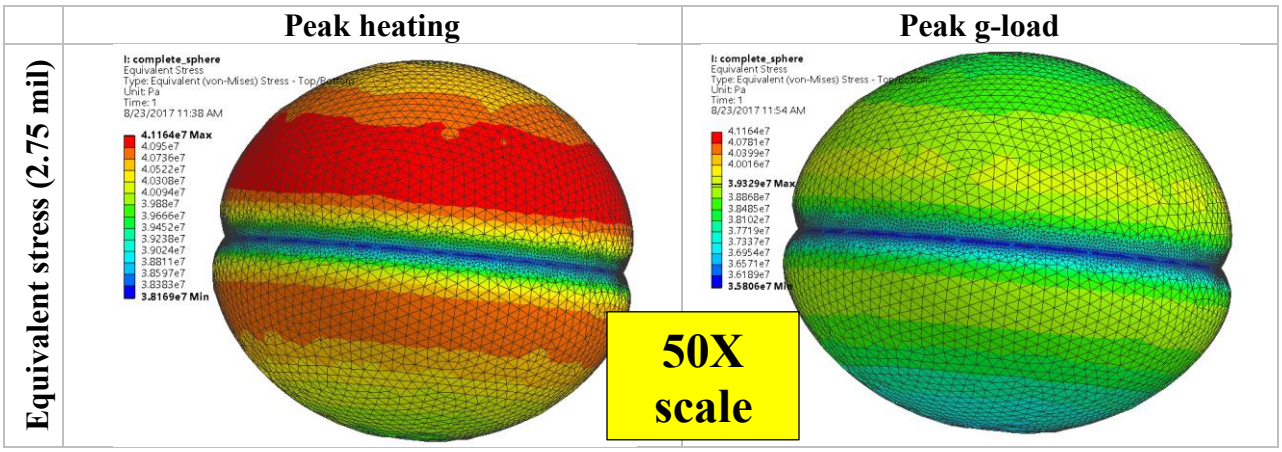

Figure 21. FEA solutions for the 70 µm (2.75 mil) thick, 80-m diameter envelope projected on the structural mesh.

In the left column, the peak results at peak heating are shown, and on the right are the results for peak g-load. The true scale inward deformation, 50X scaled inward deformation, and equivalent stress fields are shown on the ANSYS mesh. Deformations are exaggerated and indicate slight longitudinal compression and inward deformation at the equator.

7.2 Aeroelastic Modeling

Aeroelasticity is the study of the interaction between a flowing fluid and a flexible structure. In certain conditions, a feedback mechanism between the structural natural modes and the flow can cause violent instabilities. The two primary aeroelastic instabilities include flutter and divergence (buckling). The primary objective of the aeroelastic modeling analysis is to (1) characterize flutter of the thin envelope material that could occur during entry and descent and (2) determine if it could possibly cause damage to the envelope.

Flutter of thin panels and shell structures, such as thin envelopes, can usually be mitigated by increasing the effective structural stiffness. This can be accomplished in two ways: increasing the stiffness (and thus mass) of the envelope material, or increasing the static pressure across the envelope. The pressure differential will induce tensile stresses in the plane of the material which will result in increased stability. The pressure differential will be the primary parameter of interest here since we will not be examining changes to the material stiffness.

This aeroelastic analysis uses a greatly-simplified first-order analytical model. The large, thin structure is challenging to simulate accurately. A representative aeroelastic simulation would require hypersonic CFD coupled with a structural model such as an FEA. This is complex and time intensive. Our goal here is to get a general sense of the kinds of behavior we could expect and where in the entry trajectory this behavior could occur.

Pluto entry with a very large envelope is a unique situation with respect to aeroelasticity due to the extremely low density of atmospheric gas. We estimate the mean free path of Nitrogen molecules to be about 40 cm at peak heating. With most structures this would be in the free molecular flow regime, but the large envelope size relative the mean free path makes this situation effectively continuum. The low dynamic pressures (20-30 Pa), low atmospheric densities, and high Mach numbers suggest that aeroelastic flutter is not as much of a concern as it would be with more convention aerospace structures and atmospheres. In any case, we provide a simple analysis here.

7.2.1. Aeroelastic Model Assumptions

The assumptions in this analysis are as follows:

- Quasi-steady supersonic aerodynamics (Piston Theory)
- Thin shallow shell structural model for an "aeroelastic surface" with simple support boundary conditions
- Thermal effects on material stiffness neglected
- Flow separation and flow recirculation neglected

7.2.2. Aeroelastic Model

The aeroelastic model follows from the work of Dowell [9] and Goldman [10] [11]. The equations of motion are derived from first principles using a Rayleigh-Ritz energy approach. The displacements of the thin structure are written as expansions in the assumed natural mode functions. The process is rather involved and will not be reproduced here. The result is an eigenvalue problem for aeroelastic stability that is written as:

$$[p^2\boldsymbol{M} + p\boldsymbol{C} + \boldsymbol{K}]\hat{q} = 0 \qquad (3)$$

Where $\boldsymbol{M}$, $\boldsymbol{C}$, and $\boldsymbol{K}$ are the mass, damping, and stiffness matrices, respectively, $\boldsymbol{p}$ is the frequency eigenvalue and is a vector of modal coordinates. When the real part of the eigenvalues change sign, we will find coalescence of two structural natural frequencies and a bifurcation instability.

The geometry of the aeroelastic model and the entry flow characteristics are illustrated in Figure 22. The aeroelastic surface which is to be analyzed here is in the supersonic, attached flow regime only, since piston theory for aerodynamic pressure is not valid in subsonic and transonic flows.

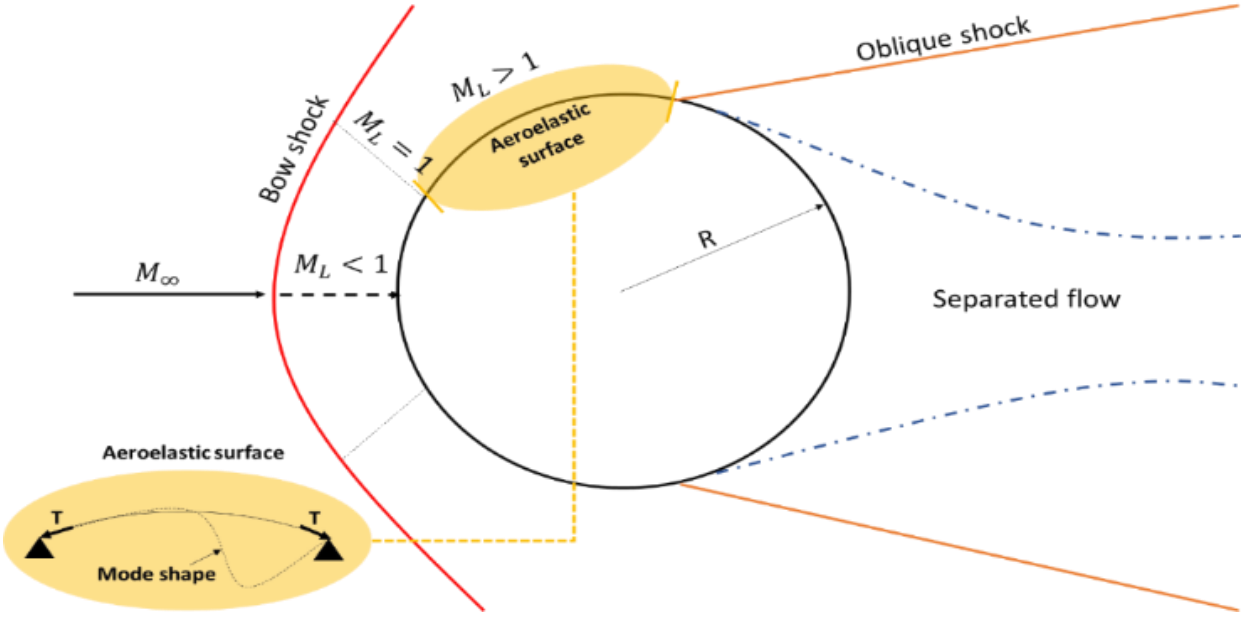

Figure 22. Aeroelastic model geometry.

The model geometry shows a circular cross section of the sphere with bow shock in front of the stagnation point and oblique shocks at the flow separation region near the rear of the decelerator. The local Mach number is

subsonic directly behind the bow shock and transitions back to supersonic moving tangentially along the surface. The aeroelastic surface is indicated in this supersonic region.

7.2.3. Aeroelastic Test Cases

To determine where in the trajectory to perform the aeroelastic calculation, we plotted the dynamic pressure, q_∞, divided by the Mach number, M. This quantity is proportional to the magnitude of the aerodynamic pressure term in the aeroelastic equations of motion and it indicates where flutter is more likely to occur. A plot of q_∞/M_∞ is given in Figure 23. The peak in the curve indicates where flutter probability is increased. Here the peak occurs around Mach 25 at an altitude of about 150 km well after peak heating and peak dynamic pressure. While this plot does not tell us if flutter occurs, it suggests the initial flow conditions to assume in the aeroelastic model.

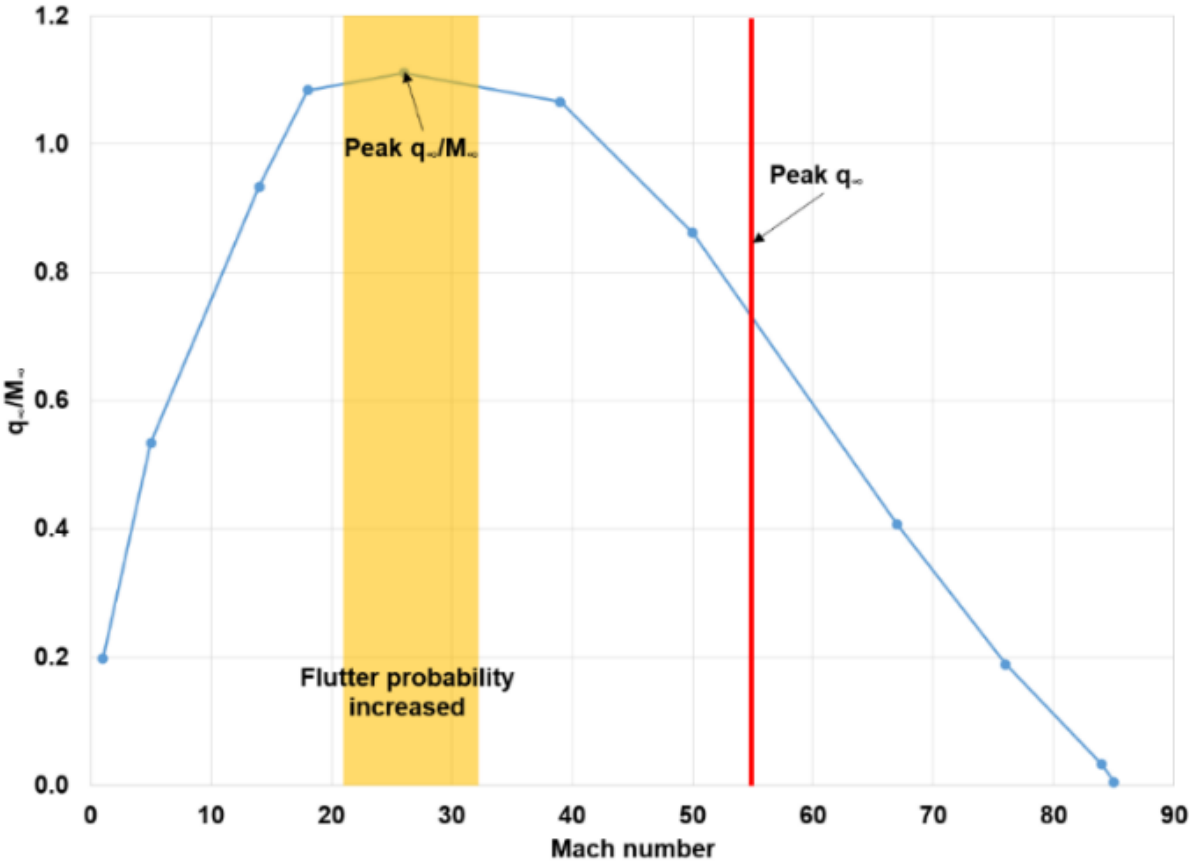

Figure 23. Plot of free stream dynamic pressure divided by Mach number.

A curve of dynamic pressure divided by Mach number for Mach numbers ranging from 0 to 90. The peak dynamic pressure is indicated at Mach 55 and the peak in the curve is indicated at Mach 25 where the flutter probability is increased.

7.2.4. Aeroelastic Results

The key flutter results are summarized in Figure 24 for the peak q_∞/M_∞ point in the trajectory. On the left, the flutter dynamic pressure is shown for various local Mach numbers in relation to the flow dynamic pressure. The flutter dynamic pressure is always greater than the flow dynamic pressure within the range of expected inflation pressures, indicating that the envelope will not

flutter. The local Mach number is unknown but is expected to be low supersonic, and this has only a minimal effect.

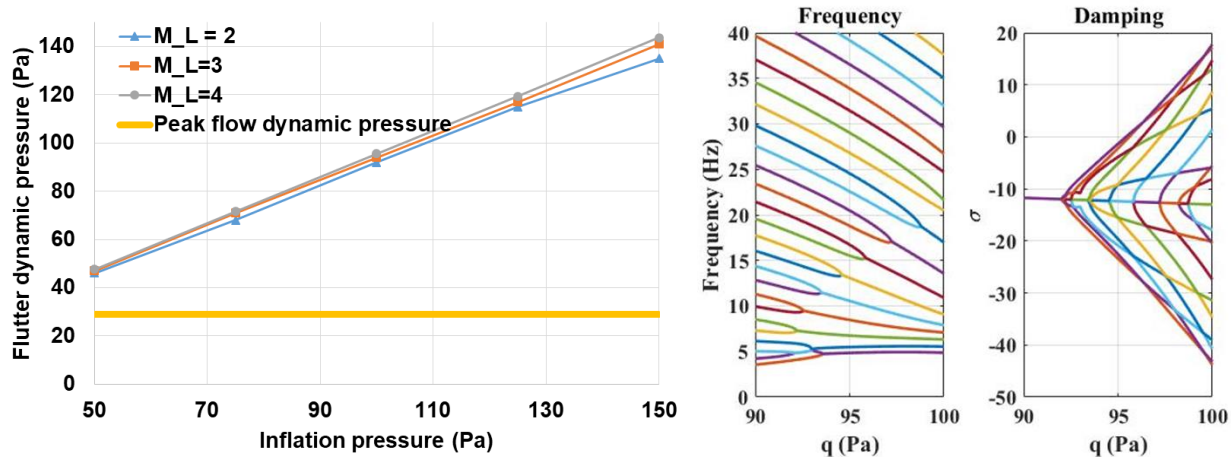

Figure 24. Flutter dynamic pressure as a function of envelope inflation pressure for various supersonic local flow Mach numbers (left), and frequency-damping plot showing the coalescence of natural modes.

The flutter dynamic pressure increases from about 45 to 140 Pa in the range of inflation pressures from 50 to 150 Pa. The peak flow dynamic pressure is indicated at 30 Pa. The frequency-damping plot shows the coalescence of natural modes and positive system damping at the flutter point.

The right plot in Figure 24 shows how the natural frequencies and system damping change as a function of dynamic pressure. We see that pairs of modes merge together in a phenomenon known as modal coalescence. Flutter occurs at the dynamic pressure where the system damping, σ, becomes positive.

7.2.1. Aeroelasticity Conclusions

We've developed a simple aeroelastic model for the Pluto decelerator envelope with several simplifying assumptions. The model indicates that the envelope is not likely to flutter during entry at Pluto since the flutter dynamic pressures are greater than the flow dynamic pressures in the range of expected envelope inflation pressures. Additional work is needed to better characterize the flowfield and more accurately represent the envelope structure. However, based on the extremely low atmospheric densities encountered during entry, catastrophic flutter that is typically seen with traditional aircraft structures is unlikely to occur here.

7.3 Aerothermodynamics Analysis

In an effort to better characterize the aerodynamic heating environment during Pluto entry, we performed an aerothermodynamics CFD analysis. The primary objective of the aerothermodynamics analysis was to (1) determine the envelope heat fluxes and temperatures during entry and (2) validate the use of conventional envelope materials and fabrication techniques.

Initially we were concerned about radiative heating since first order calculations using the Tauber-Sutton model [12] predicted relatively high fluxes that would necessitate more significant envelope materials development. A higher level of fidelity was needed to pin down radiative heating and also verify HyperPASS's Sutton-Graves predictions of convective heating.

We began this analysis using the NASA Langley Aerothermodynamic Upwind Relaxation Algorithm (LAURA) [13]. LAURA solves the flowfield in thermochemical nonequilibrium where molecular species dissociate and ionize as a result of shock layer heating. The results presented here are preliminary and further CFD convergence and mesh refinement studies are needed to assure accurate prediction.

7.3.1. LAURA Assumptions

The assumptions in this analysis are as follows:

- 100% N_2 atmosphere with species N_2, N, N+, N_2+, and e-
- Envelope surface is super-catalytic; the species mass fractions are set to free-stream conditions (this is the default in LAURA)
- Envelope surface is in radiative equilibrium
- The analysis is axisymmetric with a hemispherical grid

7.3.2. Simulation Setup and Solution Process

We used the LAURA *Self-Start* utility to build the grid and generate the input files. The volume mesh and surface grids are shown in Figure 25. The hemispherical, axisymmetric grid runs from the stagnation point to the flow tangency point along the streamwise centerline. Figure 26 shows the LAURA solution process that was used to compute convective and radiative heating. We first compute the convective solution, converge the boundary layer through a series of restarts, and restart again with radiation enabled until convergence is attained.

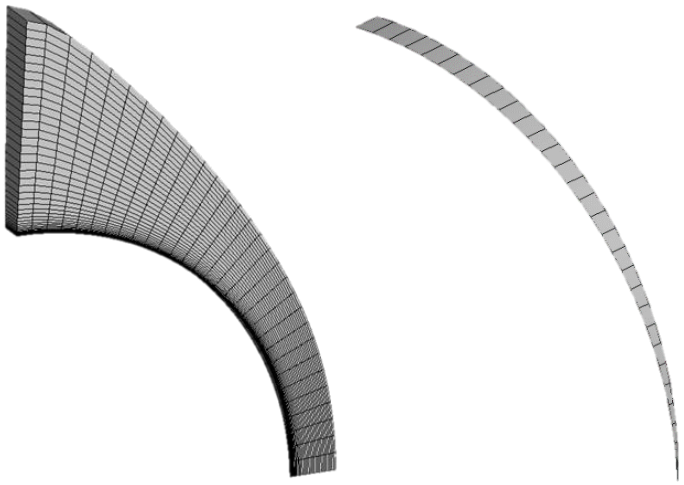

Figure 25. LAURA volume mesh (left) and surface grid (right).

The LAURA volume mesh is the discretized fluid domain. The domain is axisymmetric and hemispherical and spans from the stagnation point to the tangency point. The mesh is composed of a structured array of 3-D cells. The surface grid also runs from the stagnation point to the tangency point but uses 2-D surface elements.

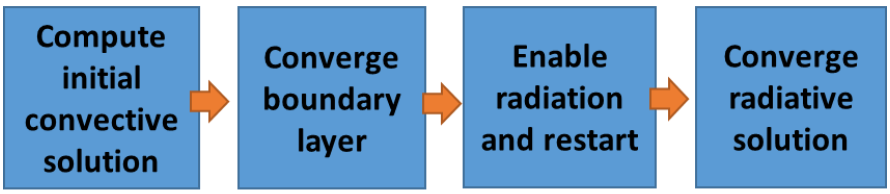

Figure 26. LAURA solution process.

The LAURA solution process as described in this figure is to (1) compute the initial convective heating solution, (2) converge the boundary layer, (3) enable radiation and restart, and (4) converge the radiative solution.

7.3.3. CFD Test Cases

Due to schedule constraints, we were only able to analyze the 70-m diameter case. This is the worst case for convective heating. We took the trajectory data from HyperPASS and chose several points in the region of the HyperPASS heat pulse to compare with LAURA results. The parameters for these points are shown in Table 3. The Pluto altitude at which the heat pulse occurs is around ~250 km. Peak convective heating as predicted by HyperPASS occurs at 131.7 s in the entry starting at 1600 km and 14 km/s. The Knudsen numbers of about 0.005 (mean free path, 0.4 m, divided by characteristic length, 80 m) indicate that the decelerator is in continuum flow regime during peak heating, whereas Knudsen numbers >0.01 indicates continuum does not hold.

Table 3. HyperPASS trajectory parameters (in heat pulse) used in LAURA simulations.

HyperPASS Simulation time (s)	Velocity (m/s)	Atmospheric Density (kg/m^3)
118.7	13580	7.17E-08
121.7	13380	1.00E-07
131.7	12110	3.06E-07
141.7	9796	6.60E-07

7.3.4. LAURA Results

Figure 27 shows the (normalized) pressure and density field solutions near the stagnation region. The captured shock is about 45% from the surface to the inflow boundary with this grid.

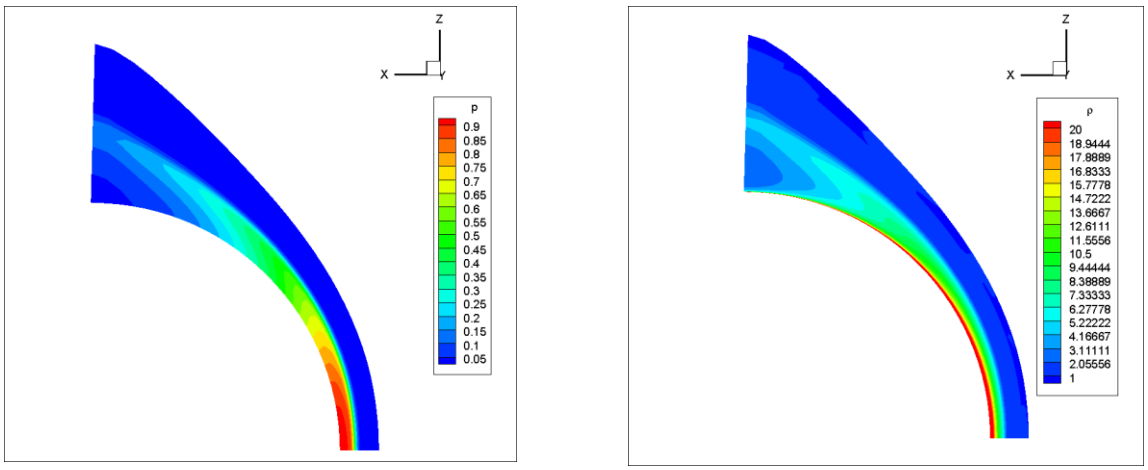

Figure 27. Static pressure normalized by (left), density field normalized by $\rho_\infty V_\infty^2$, t = 131.7 sec.

Here we show the static pressure and density contours plotted on the CFD volume mesh. The shock causes a rapid increase in static pressure near the stagnation point by a factor of 20 compared with the free stream. The density also increases by the same factor but the highest densities are seen just above the solid wall boundary.

The species mass fractions were also generated from the radiation solver and are illustrated in Figure 28. The free stream is 100% molecular Nitrogen. Behind the shock, most of the gas is dissociated into atomic Nitrogen, but there are also small fractions of monatomic and diatomic nitrogen ions and electrons. Each of these species has a contribution to the radiative heat flux seen by the envelope surface.

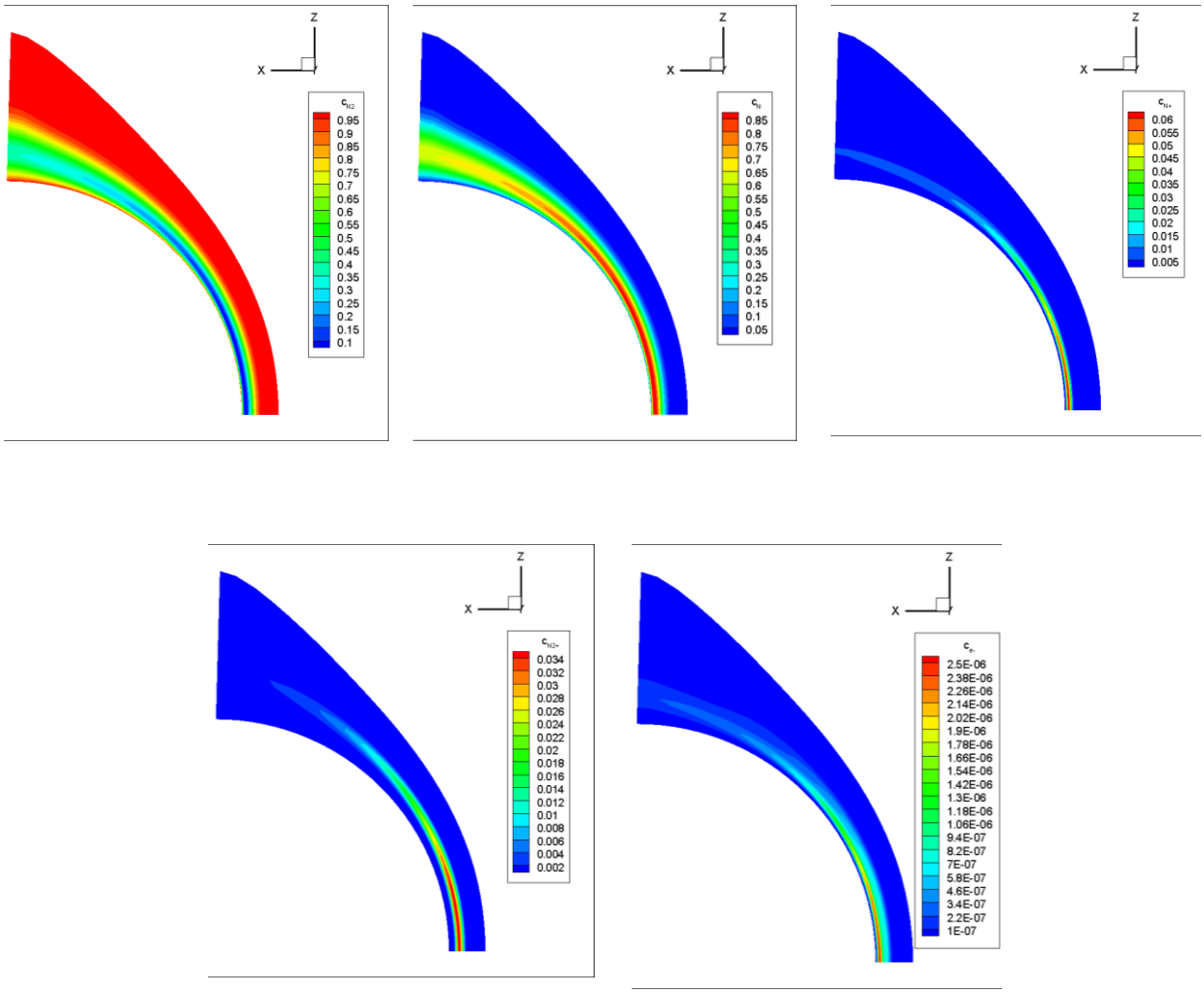

Figure 28. Species mass fractions at t=131.7 sec.

Species mass fraction contours are plotted on the CFD volume mesh. The free stream is 100% N_2. Behind the shock, we see that the N_2 mass fraction decreases to about 10% and N increases to about 90%, with small fractions of N+, N2+, and e-.

In summary, radiative heating has a very minor contribution to the total heat flux, on the order of 0.1 Watt/cm^2. We believe this to be because the mean free path of the molecules is extremely large, about 40 cm, which is nearly 1 billion times the molecular diameter. Note that the large size of the decelerator keeps the Knudsen number less than 0.01 during peak heating, which means the flow is a continuum.

The total heat flux is illustrated in Figure 29. LAURA confirms the time of the peak heating conditions predicted by HyperPASS (Sutton-Graves heating model), namely 131.7 s. All other times in Table 3 result in lower heating rates. The results show that the heating rates decrease by about a factor of 7 from the stagnation point to the flow tangency point.

LAURA's peak heat flux is about 3.5 W/cm^2, which is slightly higher than the HyperPASS result for the 70-m envelope (a direct comparison with HyperPASS is given in Figure 30). This results in peak temperatures of about 550°C (neglecting internal convection). This temperature is lower than what would be seen by a solid surface because the thin envelope can radiate heat from both sides since the film is so thin. The temperature profile in K (neglecting internal convection) is shown in Figure 31.

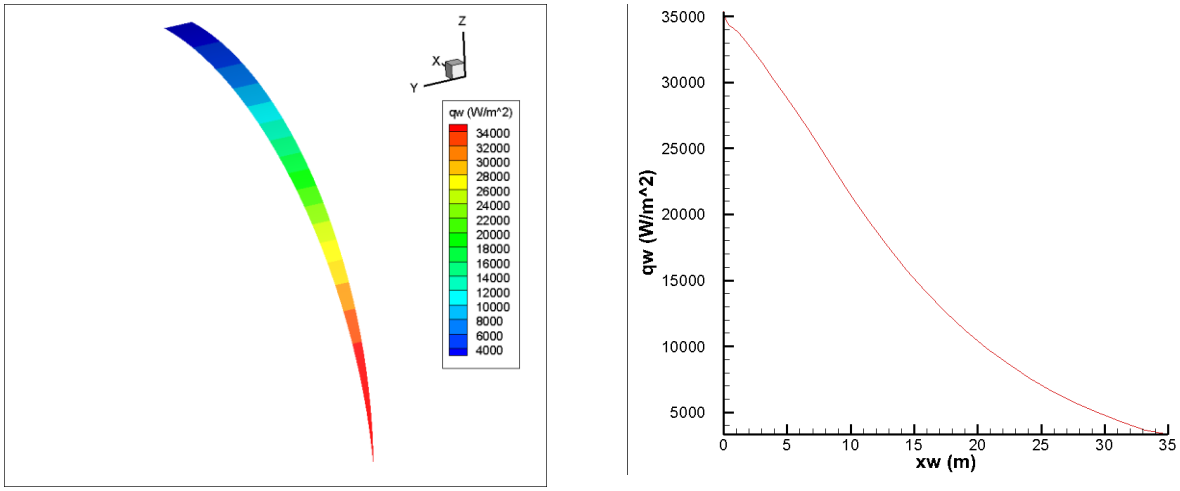

Figure 29. Heat flux surface profiles, t=131.7 s.

The surface heat flux profile as plotted on the CFD surface grid indicates peak heating at the stagnation point of 3.5 W/cm^2 that gradually decreases to 0.4 W/cm^2 at the flow tangency point of the sphere.

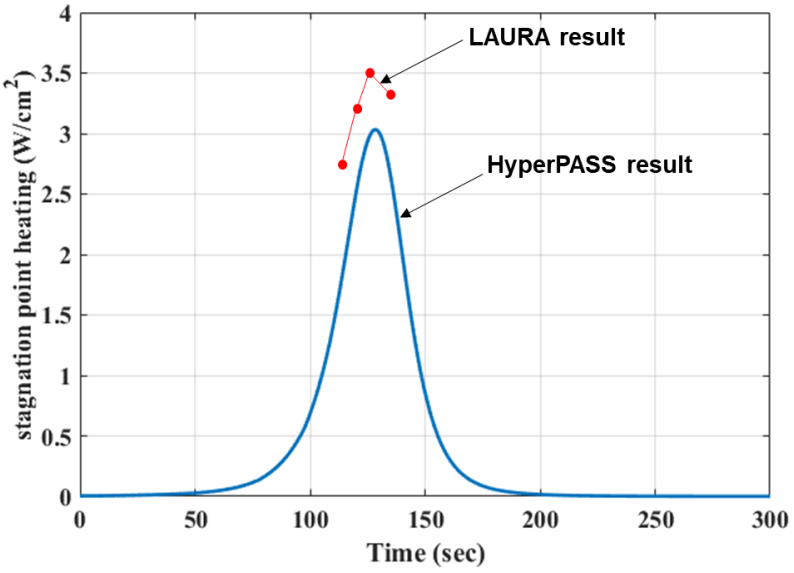

Figure 30. Comparison between the LAURA and HyperPASS heating rates for the 70-m envelope.

This figure shows that the LAURA predictions are about 0.5 W/cm^2 higher than the HyperPASS result.

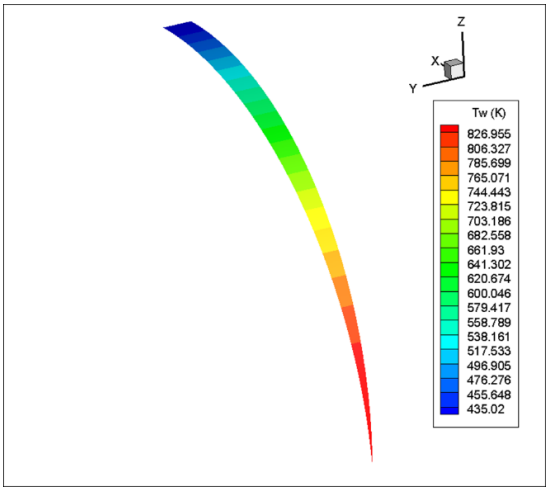

Figure 31. LAURA surface temperature profile, t=131.7 sec.

The surface temperature profile as plotted on the CFD surface grid indicates peak temperature at the stagnation point of 826 K (550°C) that gradually decreases to 435 K (160°C). Internal convection is neglected so these temperatures are overestimates.

7.3.5. Aerothermodynamics Analysis Conclusions

The LAURA CFD results support the earlier HyperPASS predictions and further confirm the feasibility of the EAD decelerator design for Pluto entry. Results show that radiative heating is a small fraction of the total heat flux and convective heating is very low, well within the thermal capabilities of existing thin film materials. However, further work is still needed to verify simulation predictions and assure convergence has been attained for all simulation cases.

7.1 Envelope Thermal Analysis

The objective of the thermal analysis of the decelerator was to determine the transient entry temperatures of key elements including the envelope surface, inflation gas, and base cap structure. The transient inflation gas temperature is particularly important for determining the inflation pressure that must be large enough to keep the envelope inflated during deceleration and low enough to not cause dangerous membrane stresses. Two methods were used to analyze the internal convection of the inflation gas: (1) A first-order analytical model and (2) CFD simulation. Our past experience indicated substantial uncertainty in first-order internal convection modeling so that is why we decided to use CFD for an additional convection analysis here.

7.1.1. Thermal Analysis Assumptions

The following assumptions were used in the first order model for the envelope, gas, and base cap:

- For the internal convection model, the envelope is considered a single node with a uniform average temperature across the entire sphere
- The quiescent gas temperature (far from surface) is uniform in the envelope internal volume
- Initial temperature of all components is 300 K

- Internal surface-to-surface radiation is neglected

The following assumptions were used in the CFD model for the gas:

- At each transient solution, the envelope surface temperature is held constant
- Laminar flow viscous model
- Radiation view factors for the internal surface calculated using the Surface to Surface (S2S) model

7.1.2. Thermal Analysis Theory

The theory for the first order thermal model derives from past work at Caltech and JPL [14]. The transient temperature of the gas inside the envelope is given by:

$$m_{gas}C_{v,gas}\frac{dT_{gas}}{dt} = hA(T_{env} - T_{gas}) \quad (4)$$

And the envelope surface temperature is given by:

$$m_{env}C_{env}\frac{dT_{env}}{dt} = hA\left(T_{surf} - T_{gas}\right) + \epsilon\sigma AT_{env}^4 \quad (5)$$

The internal convection coefficient h is related to the Nusselt number by $Nu = hD/k$. The Nusselt number correlation used here is given by Carlson and Horn [15]:

$$Nu = \begin{cases} 2.5(2 + 0.6Ra^{0.25}) & Ra < 1.35\ x\ 10^8 \\ 0.325Ra^{0.33} & Ra > 1.35\ x\ 10^8 \end{cases} \quad (6)$$

The Rayleigh number is defined in the standard manner using the envelope diameter as the characteristic length. Equations *(4)* and *(5)* are coupled 1st order ODEs and are easily solved in Excel using the Euler method. The CFD internal convection theory is complex and will not be reproduced here. For more details on the thermal physics please refer to the ANSYS FLUENT documentation**. The process by which the CFD solutions were generated is as follows. Several points in 100°C increments were selected along the envelope temperature time history. A transient solution was generated at each point with a simulation time equal to the corresponding time interval between 100°C increments in the temperature time history. Each successive simulation was restarted using the solution generated at the previous point. This approach allowed us to approximate the convective dynamics of the gas over the peak heat pulse.

7.1.3. Thermal Analysis Results

The results of the first order model are given in Figure 32. The peak envelope temperature at the stagnation point is about 520°C, slightly less than the value predicted by LAURA (neglecting internal convection). The gas temperature lags behind the envelope and reaches a maximum value of about 415°C. The base cap temperature lags even further behind the envelope due to its high areal density and thermal inertia, reaching a maximum value of about 440°C. We emphasized that these temperatures are very low for an entry from interplanetary speed, which is due to the large diameter of the decelerator and the nature of the Pluto atmosphere.

** http://www.ansys.com/Products/Fluids/ANSYS-Fluent

We compared the CFD average gas temperature with the predictions of the analytical model. Figure 33 shows that there is generally good agreement, though greater deviation is seen at higher temperatures. This suggests that the analytical model formulation, particularly the convection coefficient and Nusselt number (Eq. *(6)*) captures the key physics of the system. We also examined the CFD predictions of internal pressure in relation to the deceleration time history. We see that the pressure increases with increasing deceleration. This is important because the internal pressure must keep pace with the increased compressive loads that are introduced into the envelope during deceleration in order to resist envelope deformation.

Field plots of temperature, density, and velocity are shown in Figure 34. The plots correspond to the CFD solution points in Figure 33 (left). These results illustrate the evolution of the convection process inside of the envelope during the heat pulse. The results are somewhat different from what one might find with internal convection of a gas on the surface of the Earth. This is because the effective acceleration due to the atmospheric drag is in the upward direction, opposite to the direction of gravitational acceleration on a planet. The acceleration field is a key parameter in the buoyancy model used to calculate the convection coefficients in the CFD model.

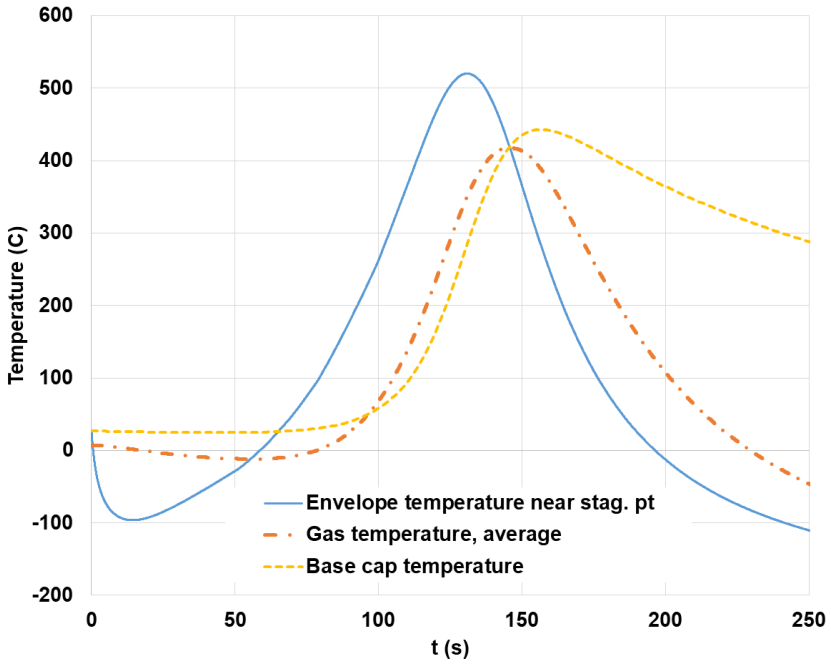

Figure 32. Envelope surface, inflation gas, and base cap temperature during entry.

The envelope temperature near the stagnation point reaches a peak of about 520°C, the volume-averaged gas temperature lags in time and reaches a peak of about 410°C, and the base cap also lags in time and reaches a peak temperature of about 440°C.

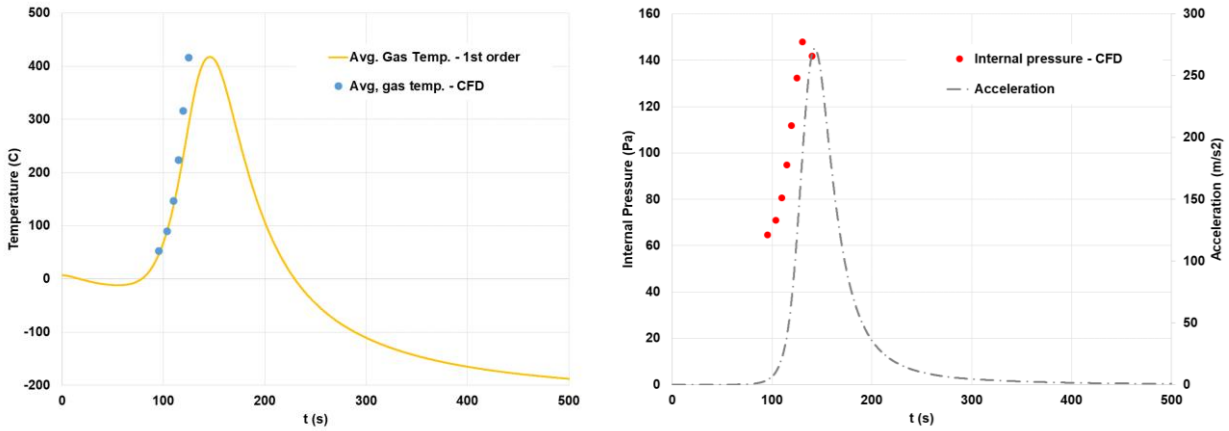

Figure 33. CFD predictions of volume-averaged inflation gas temperature compared with analytical model (left), CFD predictions of internal pressure compared with entry deceleration (right).

The volume-averaged gas temperature time history is shown for the 1st order analytical model along with CFD predictions. Peak temperature is about 410°C. The CFD results generally match up with the analytical model though some deviation is seen at higher temperatures. The CFD pressures are also shown and increase from about 60 to 150 Pa during the heat pulse. The lag time in the pressure follows the increasing acceleration that occurs a few seconds after the heat pulse.

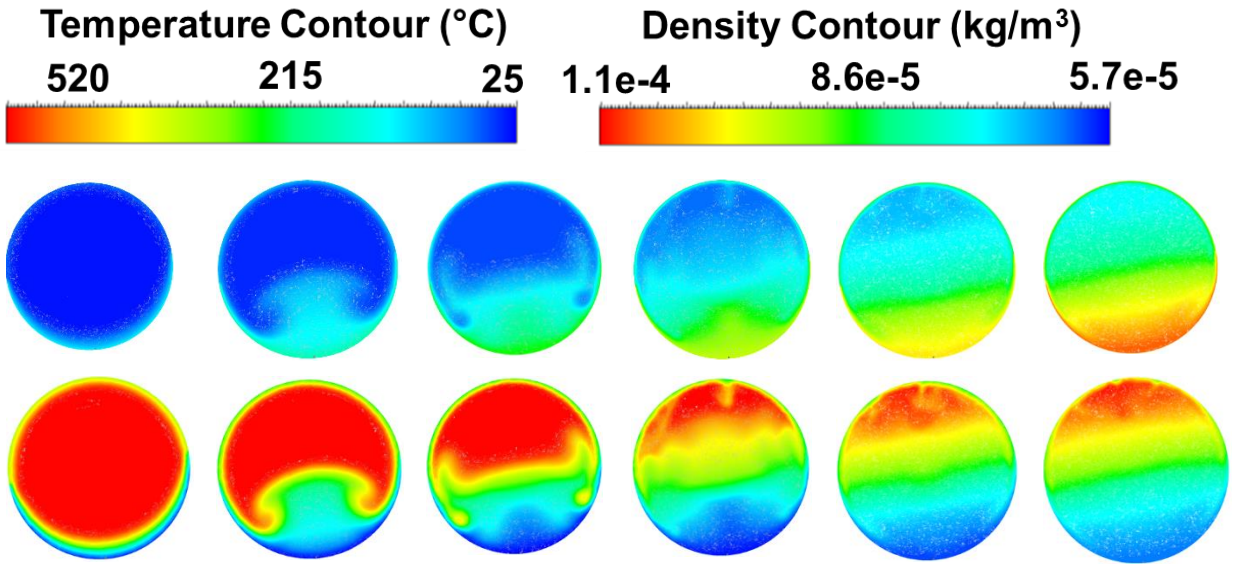

Figure 34. Field plots of temperature (top row) and density (bottom row). Time increases to the right.

The temperature and density fields plotted in a cross-section of the CFD volume mesh are shown as a function of time. The temperatures increase from the stagnation point into the rest of the volume through convection. The local peak temperature is roughly that of the surface (520°C) but the space-facing side radiates heat and keeps the top of the envelope cooler. The density field indicates a region of lower density near the stagnation point due to the increased temperature there.

7.1.1. Thermal Analysis Conclusions

During entry, the envelope, gas, and base cap temperatures range from about 400°C to 520°C. These temperatures are within the acceptable temperature ranges for potential envelope and base

cap materials at short exposure times. CFD analysis showed good agreement with the predictions of a simple analytical thermal model with two nodes. We also found that the internal pressure increases due to the increased heating and this pressure rise follows approximately the g-load profile during entry.

7.2 Decelerator Envelope Conceptual Design

In this task, we used the prior supporting analysis efforts to generate a conceptual design of the decelerator envelope. We determined that the envelope can be constructed from commercial off-the-shelf components and it can be fabricated using known and feasible softgoods industry techniques. ILC Dover was responsible for performing this subtask with guidance from GAC. Key accomplishments include:

- Materials selection
- Reinforcement feature design
- Material mass analysis
- Patterning scheme design
- Seaming design
- Load management system design
- Total envelope system mass breakdown

Due to the potential ITAR limitations on the discussion of the construction of aerodynamic decelerators, we have included the details of this tasks in a proprietary appendix.

8 Lander-Hopper Conceptual Design

In this task we generated a conceptual lander-hopper design and produced a component mass breakdown. The objective of this task was to (1) create CAD drawing at the system level and (2) generate a system-level mass breakdown. In the next sections we'll briefly discuss the conceptual lander-hopper system design.

Prior to separation from the decelerator, lander-hopper performs all the functions of a typical cruise stage. It contains all the subsystems necessary for power, communications, propulsion and attitude control, and thermal control. A thermal radiator, required keeping the lander-hopper cool during cruise, and envelope inflation tanks are jettisoned after envelope deployment and inflation. After entry, and upon reaching terminal speeds just above the surface, the lander-hopper is separated from the envelope, translated horizontally via thrusters away from the envelope, deploys its landing legs and configures its subsystems for the final main engine propulsive burn and landing. Figure 35 illustrates the lander-hopper on the surface of Pluto with its high-gain antenna pointed toward the Earth. The same main engine and thrusters are used to hop around the surface. Hopping is particularly efficient on Pluto since the gravitational acceleration is low, just 0.06 gee, and atmospheric drag at low speeds is minimal.

Lander-hopper subsystems consist of command and control, structure, power, communications, propulsion and attitude control, thermal control and science. These are discussed further in the next sections.

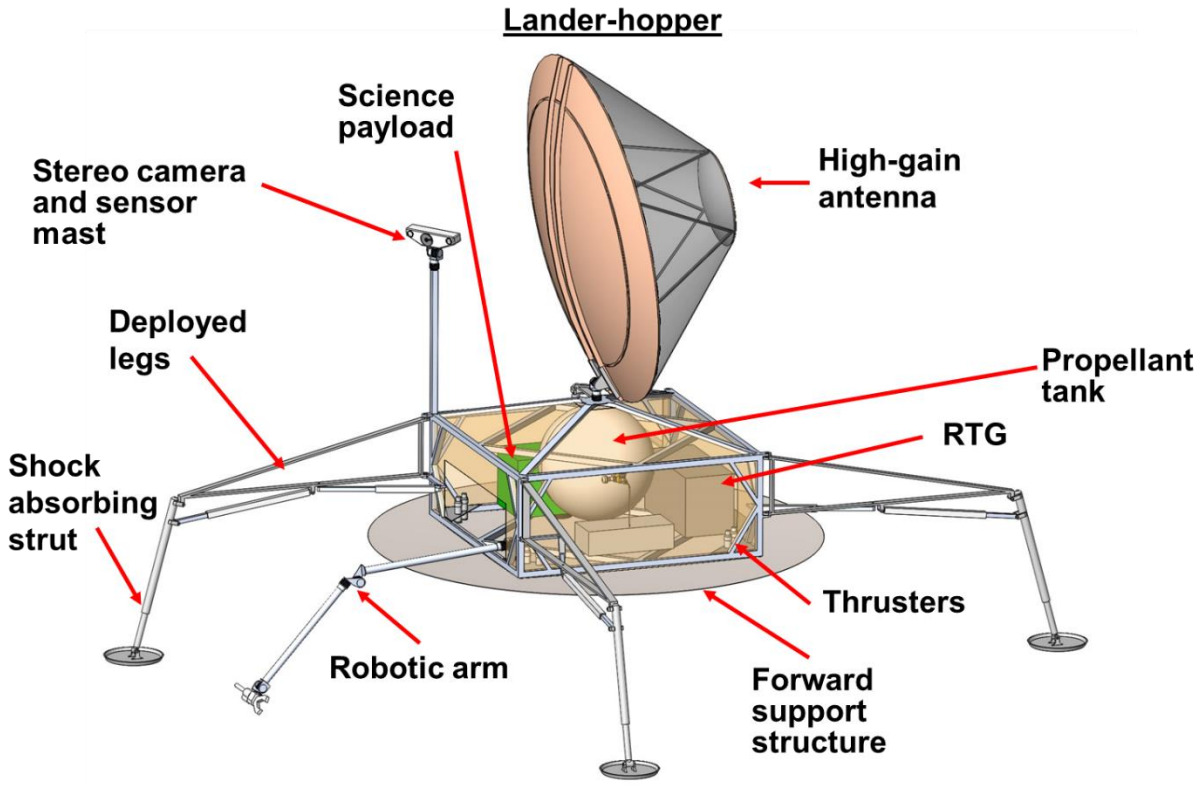

Figure 35. Lander-hopper conceptual design.

The lander-hopper design concept shows the locations of key subsystems on the craft including the science payload, high-gain antenna, propellant tank, RTG, thrusters, forward support structure, robotic arm, shock absorbing struts, deployed legs, and stereo camera and sensor mast.

8.1 Command and Control Subsystem

The command and control subsystem consists of redundant computers, memories, and interface electronics. This subsystem stores commands, sequences, science and engineering data and executes commands to the various subsystems.

8.2 Structure Subsystem

A key element of the support structure is the Forward Support Structure (FSS) to which many components are mounted and through which all entry loads are connected to the envelope. In the integrated Entrycraft architecture, the windward end of the decelerator is the FSS. It also functions as the envelope base for the decelerator. The FSS is illustrated in Figure 35. This structure is envisioned as a 2-m diameter, insulated, titanium spherical cap with a radius of curvature equal to that of the envelope. The FSS is insulated to protect lander components on the opposite side of the entry interface and made of titanium to take the entry loads. Aluminum may also be an option depending on the strength of aluminum at the stagnation temperatures expected. This structure seals the envelope and protects and supports the remaining lander structure and subsystems during cruise and entry, and provides attachment for deployable landing legs and a frame. It also interfaces with the base fitting on the envelope and includes a separation mechanism that is activated prior to landing. Conceptually, the lander-hopper subsystems are contained within a box-like structure behind the FSS. The structure

8.3 Power Subsystem

One Multi-Mission Radioisotope Thermoelectric Generator (RTG), currently in production by the DOE powers the craft. This unit provides 100 W EOL power to the science payload and other subsystems. The RTG is connected to a radiator used during cruise and also has the ability to radiate out the side of the lander-hopper structure once on the surface. A small secondary battery provides higher instantaneous power when required of lander-hopper subsystems.

8.4 Communications Subsystem

Communications to Earth is enabled by a large (~2-m) high-gain parabolic antenna with an elevation/azimuth pointing system. An X-band radio, similar to *New Horizons*, is also assumed. The pointing of the antenna is achieved by rotation about the azimuth by means of an actuator and about the elevation direction by another actuator. Different elevation angles are obtained by running the actuator along the geared backside of the antenna. One or more small omni-directional and/or low-gain antennas will be used during cruise when the Entrycraft needs to point its antenna away from Earth for propulsive maneuvers or when it needs to re-orient its spin axis for entry.

8.5 Propulsion and Attitude Control Subsystem

The propulsion and attitude control subsystem consists of several small attitude thrusters (1 and 5 N) and a main engine (275 N) all using monopropellant hydrazine (I_{sp} = 240 s) for propellant. A set of thrusters on the forward support structure will be used for attitude control during cruise, landing and hopping and the main engine will be used for large trajectory correction, landing and hopper maneuvers.

We have allocated 30 kg of hydrazine for hopping, separate from the propellant required for cruise propulsion and attitude maneuvers and the landing burn. With this propellant mass, the lander-

hopper could travel a maximum distance of about 50 km. In Table 4 we show various options for hopping maneuvers and the distances traveled. These calculations include the deceleration propellant requirements.

Table 4. Lander-hopper trajectories for various hop delta-Vs. 30 kg propellant store.

Delta-V (m/s)	Maximum height (m)	Horizontal range (m)	Number of hops allowed with propellant store
10	40	160	17
18	130	522	10
25	252	1,008	7
50	1,007	4,032	3
100	4,029	16,130	2
175	12,100	50,530	1

8.6 Thermal Control Subsystem

During cruise and after landing, lander-hopper subsystems will be kept at acceptable temperatures using a combination of good insulation and the use of RTG waste heat (~2000 W). During cruise, excess RTG heat will be radiated out the forward support structure via a separate radiator that will be jettisoned prior to entry. During entry, an insulation layer behind the forward support structure, component heat capacity, and the low-pressure environment in the envelope mitigates lander-hopper temperature rise due to aeroheating. Figure 32 shows that the forward support structure (base cap) surface temperature only reaches about 440°C during entry. Once at the surface, the RTG no longer radiates via the radiator on the forward support structure since it has been jettisoned prior to entry. Instead, the RTG waste heat is radiated out the side of the lander-hopper.

8.7 Science Instrumentation

Notional science instruments include a surface heat flow and physical properties package, a seismometer to measure tidal flexing, 8 stereo cameras, aerothermal and radiometer sensors, geophysical sounding system, gas chromatograph mass spectrometer, robotic arm, and an atmospheric sensing suite. A mass and power breakdown is given in Table 5.

Table 5. Lander-hopper science package mass and power breakdown.

Description	Mass, CBE (kg)	Power, CBE (W)
Heat Flow and Physical Properties	1.8	5.0
Seismometer - Tidal Flexing	6.0	1.8
Stereo Cameras	1.5	17.6
Aerothermal and radiometer sensors	1.7	4.5
Geophysical Sounding System	1.2	5.0
Gas Chromatograph Mass Spectrometer	10	50.0
Robotic Arm	5.0	28.0
Atmospheric Suite	1.5	2.0
Total	27.7	108.9

8.8 Lander-Hopper Mass Breakdown

We have generated a conceptual lander-hopper mass breakdown that includes current best estimate (CBE) values and maximum expected values (MEVs). This is given in Table 6. Based on the decelerator mass and entry mass limitations discussed earlier, our objective is to keep the lander-hopper mass on the surface below 200 kg total. While the CBE meets this requirement, the MEV is slightly higher. Further work will be needed to refine the lander-hopper design and possibly de-scope some capabilities in order to meet the entry mass requirements.

Table 6. Lander-hopper mass breakdown.

Qty	Description	Unit CBE Mass, kg	Subtotal CBE Mass, kg	Contingency %	Contingency Mass, kg	MEV, kg
	Command and Control Subsystem					
1	Flash LIDAR Surface Scanner	1.4	1.4	20%	0.3	1.7
1	Control Electronics	0.5	0.5	30%	0.2	0.7
	Total Mass Command and Control Subsystem Only		**1.9**		**0.4**	**2.3**
	Structure Subsystem					
1	Frame	11.0	11.0	20%	2.2	13.2
1	Body Panels	1.0	1.0	20%	0.2	1.2
1	Base Cap / Forward Support Structure	13.0	13.0	10%	1.3	14.3
1	Insulation	2.0	2.0	20%	0.4	2.4
1	Interface	4.0	4.0	20%	0.8	4.8
4	Leg Structure	0.8	3.2	30%	1.0	4.2
4	Hinge Actuator	0.5	2.0	30%	0.6	2.6
4	Leg Strut and Shock Absorber	1.2	4.8	30%	1.4	6.2
4	Strut Actuator	0.7	2.8	30%	0.8	3.6
4	Foot Pad	0.5	2.0	30%	0.6	2.6
	Total Mass Structure Subsystem Only		**45.8**		**9.3**	**55.1**
	Power Subsystem					
1	RTG Generator	45.0	45.0	20%	9.0	54.0
1	Battery Bank	1.0	1.0	50%	0.5	1.5
1	Power Supply Controller	1.0	1.0	50%	0.5	1.5
1	Cruise Radiator Interface	1.5	1.5	50%	0.8	2.3
1	Thermal Management System	2.0	2.0	50%	1.0	3.0
	Total Mass Power Subsystem Only		**50.5**		**11.8**	**62.3**
	Science Payload					
1	Heat Flow and Physical Properties	1.8	1.8	33%	0.6	2.4
1	Seismometer - tidal flexing	6.0	6.0	33%	2.0	8.0
1	Stereo Cameras	1.5	1.5	50%	0.8	2.3

Qty	Description	Unit CBE Mass, kg	Subtotal CBE Mass, kg	Contingency %	Contingency Mass, kg	MEV, kg
1	Aerothermal and radiometer sensors	1.7	1.7	40%	0.7	2.4
1	Geophysical Sounding System	1.2	1.2	40%	0.5	1.7
1	Gas Chromatograph Mass Spectrometer	10.0	10.0	40%	4.0	14.0
1	Robotic Arm	4.0	4.0	40%	1.6	5.6
1	Atmospheric Suite	1.5	1.5	40%	0.6	2.1
	Total Mass Science Payload Only		**27.7**		**10.7**	**38.4**
	Propulsion and Attitude Control Subsystem					
1	Hydrazine Fuel Tank (Surface Tension 78L Capacity)	6.8	6.8	5%	0.3	7.1
4	1N Thruster (Yaw Rotation)	0.3	1.3	5%	0.1	1.4
4	5N Thruster (Cyclic, pitch, roll)	0.3	1.3	5%	0.1	1.4
1	Plumbing	1.0	1.0	30%	0.3	1.3
1	Valves	0.8	0.8	30%	0.2	1.0
1	Propellant (Hydrazine/MON)	30.0	30.0	5%	1.5	31.5
1	Helium Pressure Gas	0.2	0.2	50%	0.1	0.3
1	275N Thruster (Main thruster, takeoff and landing	1.0	1.0	5%	0.1	1.1
	Total Mass Propulsion and Attitude Control Subsystem Only		**42.4**		**2.6**	**45.0**
	Communications Subsystem					
1	Main Dish	5.0	5.0	50%	2.5	7.5
1	Dish Pointing Actuators	1.0	1.0	30%	0.3	1.3
1	Radio Electronics	1.0	1.0	30%	0.3	1.3
	Total Mass Communications Subsystem Only		**7.0**		**3.1**	**10.1**
	Total Mass Lander-Hopper		**175.3**		**38.0**	**213.3**

9 Conceptual Integrated System Design

In this final task we generated the conceptual design of the integrated Entrycraft system. This includes a layout of the integrated system as well as a list of components needed for cruise to Pluto. The integrated entrycraft (cruise stage) mass breakdown was also generated.

Our current integrated system concept is illustrated in Figure 36. This shows the packed envelope around the stowed lander-hopper payload along with a cover that is used for envelope protection from micrometeoroids during cruise. The inner envelope sleeve is a lightweight polymer material that allows the envelope to be packed against the lander. We also show the inflation tanks and cruise stage RTG radiator.

The integrated system mass breakdown is provided in Table 7. The total launch mass maximum expected value (MEV) is about 830 kg. This leaves a 200 kg margin in launch mass based on the launch vehicle lift capacity to the required C3 of 1030 kg.

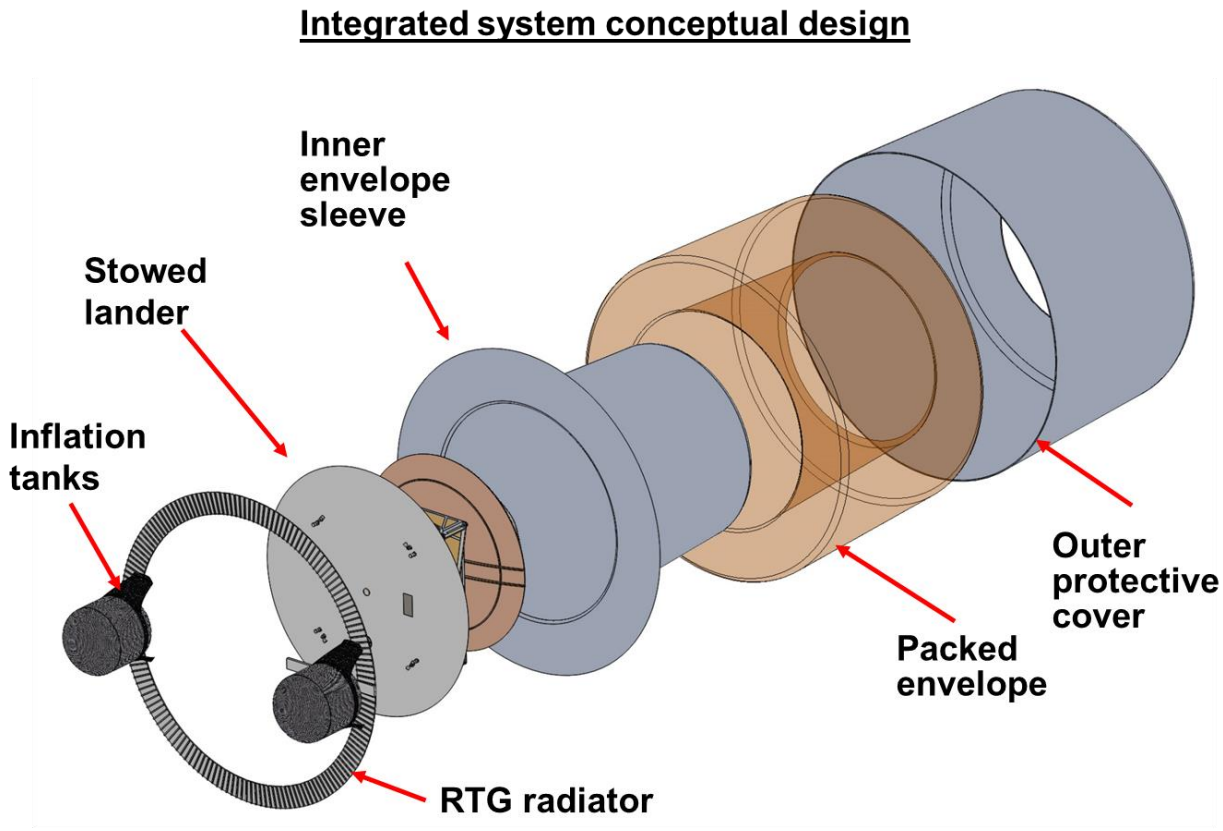

Figure 36. Integrated system conceptual design.

The integrated system includes the inflation tanks, RTG radiator, stowed lander-hopper, inner envelope sleeve, packed envelope, and outer protective cover.

Table 7. Integrated system mass breakdown.

Description	*CBE Mass, kg*	*Contingency %*	*Contingency Mass, kg*	*MEV, kg*
Total Decelerator	**353.5**	**15.7%**	**55.4**	**408.9**
Envelope components	337.5	15.0%	50.6	388.1
Inflation gas	16.0	30.0%	4.8	20.8
Total Lander-Hopper	**187.3**	**22.9%**	**42.8**	**230.1**
Lander-Hopper system	175.3	21.7%	38.0	213.3
Landing propellant	12.0	40.0%	4.8	16.8
Components jettisoned prior to entry	**185.0**	**41.1%**	**76.0**	**261.0**
Inflation tanks	100.0	40.0%	40.0	140.0
Cruise propellant	50.0	40.0%	20.0	70.0
Envelope micrometeoroid protective cover	20.0	50.0%	10.0	30.0
Cruise radiator	15.0	40.0%	6.0	21.0
Total entry mass	**540.8**		**98.3**	**639.1**
Total integrated system/launch mass	**725.8**		**174.3**	**900.1**

10 Reporting

The key reporting milestones during this Phase I effort are listed below.

- June 6-7, 2017, Attended the NIAC orientation meeting,
- September 21, 2018, Released a press release on the NIAC symposium briefing,
- September 25, 2017, Presented the concept at the NIAC Symposium,
- November 30, 2017, A briefing was given to the NASA Principal Technologist for Entry, Descent, and Landing,
- December 13, 2017, Submitted a Quarterly Report to the NIAC Program Office,
- December 19, 2017, A briefing was given to the NASA Planetary Science Division Director,
- February 8, 2018, Submitted this Final Report to the NIAC Program Office.

A compilation of published news articles on the Pluto Hop, Skip, and Jump concept is shown in Figure 37.

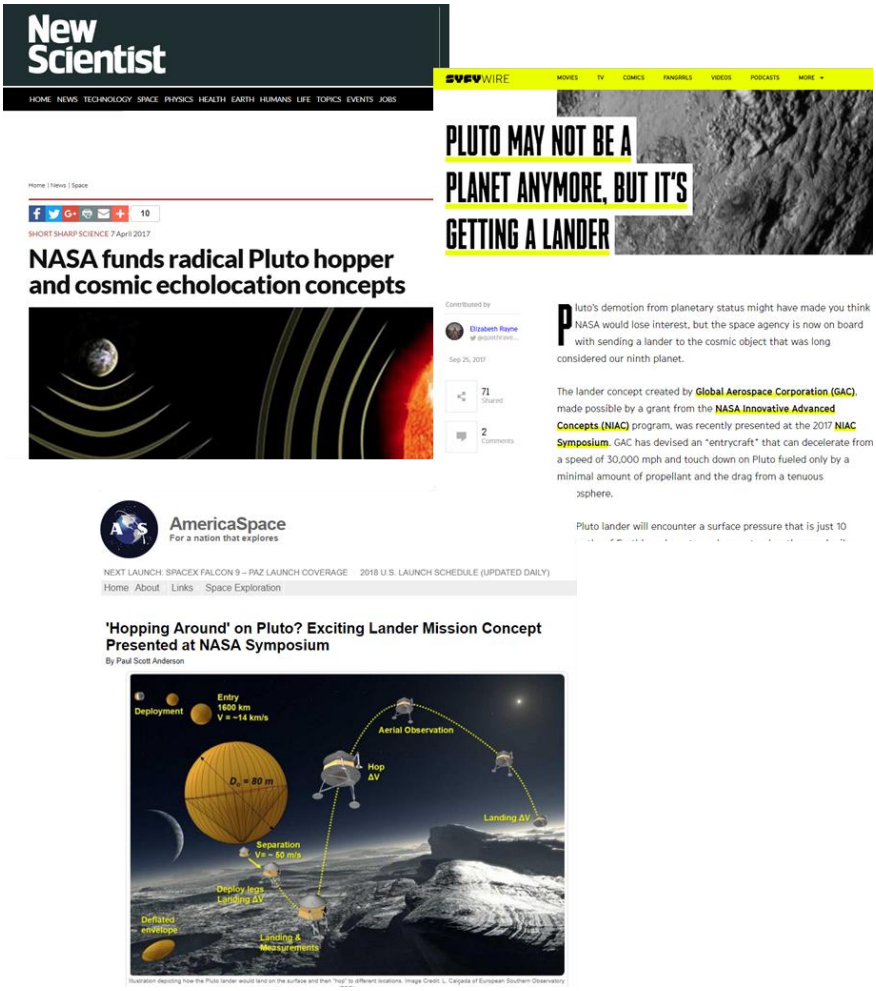

Figure 37. News articles published on the Pluto Hop, Skip, and Jump Concept.

Publications include New Scientist, SyFy Wire, and AmericaSpace.

11 Conclusions

In this Phase I NIAC effort, we developed the conceptual design of an *Entrycraft* architecture that can be used to deliver a lander-hopper to the surface of Pluto or insert an orbiter via aerocapture making such missions a real possibility within the current *New Frontiers* mission program.

Analysis showed that the primary innovation, a large inflatable envelope, is likely to be a feasible method for entry and deceleration at Pluto from high interplanetary speeds. Momentum exchange with nitrogen molecules in the existing, low-density atmosphere of Pluto enables this innovation to eliminate the need for significant and expensive onboard RTG power for electric propulsion deceleration. Only 1 MMRTG is required to power the cruise and lander systems. This is in contrast to other proposed system for Pluto deceleration that require kilowatts of power from nuclear power sources that have not yet been developed. Below we summarize the conclusions from each of the major tasks in this Phase I effort.

In Task 1, we refined atmospheric models using the most recent *New Horizons* measurements and established the system-level requirements for a reference mission design. Research on the Pluto atmosphere indicated that is does not collapse as once thought, and models show that it is expected to increase in density in the current epoch. A reference interplanetary trajectory was generated using a point-to-point conic method. The Earth launch date is January 4, 2029, Jupiter assist, on July 2, 2030, and Pluto arrival, September 11, 2040. The total flight time is 11 years 8 months.

In Task 2, we used first-order planetary aeroassist simulations to study the Pluto entry environment conditions including convective heating, g-loads, dynamic pressures, and evaluated the effect of atmospheric variation on the decelerator performance. Peak convective heating was on the order of 3 W/cm^2, g-loads of about 27, and dynamic pressures near 30 Pa. Deceleration at Pluto from 14 km/s is feasible even with atmospheric variation of ±50% in density. Entry masses of 400-700 kg are feasible for envelopes 70 – 80 meters in diameter. Next, we analyzed approach and landing conditions to determine the possible Pluto landing site locations based on the arrival geometry, and we also performed an analysis of aerocapture to evaluative feasibility of using the EAD decelerator concept for orbit insertion. Several landing sites in the northern hemisphere can be accessed. Aerocapture is also possible with the correct entry flight path angle and thrust maneuvers. Similar to observations done in support of the *New Horizons* mission, Earth-based stellar occultations may be needed to provide atmospheric characterization prior to final entry targeting.

In Task 3, we first performed analysis in support of developing the conceptual deceleration design. This includes static structural, dynamic aeroelastic, CFD aerothermodynamics, and thermal analysis. We found that the envelope does not deform significantly due to inward payload forces applied at the equator. Low order aeroelastic analysis suggested that flutter is unlikely as long as the envelope inflation pressure is greater than the dynamic pressure. Aerothermodynamics simulations using NASA's LAURA CFD indicated heating rates that were commensurate with those predicted by first order methods, about 3.5 W/cm^2. LAURA surface temperatures peaked at 550°C (without internal convection). Thermal analysis including convection of the inflation gas indicated peak envelope temperatures of 520°C. Using these results, ILC Dover generated the decelerator envelope design including material, reinforcement, seaming, patterning, and load management concept.

In Task 4, we developed the conceptual design of a lander-hopper, selected a notional science payload, evaluated hopper performance at the surface, created CAD drawing of the system, and generated a mass breakdown.

In Task 5, we developed the integrated system conceptual design and mass breakdown.

The bottom line result from this study can be summarized with the following: **There may be a *New-Frontiers*-class mission for a Pluto lander, and possibly for an orbiter, with a launch opportunity in 2029.**

12 References

[1] C. Olkin, "Evidence that Pluto's atmosphere does not collapse from occultations including the 2013 May 04 event," *Icarus,* vol. 246, pp. 220-225, 2015.

[2] G. Robuchon and F. Nimmo, "Thermal evolution of Pluto and implications for surface tectonics and a subsurface ocean," *Icarus,* vol. 216, no. 2, pp. 426-439, 2011.

[3] B. Goldman, *Private Communications with Randy Gladstone,* Irwindale, CA, 2017.

[4] A. McRonald, K. Gates and K. Nock, "Analysis of High-speed Aerocapture at Mars Using HyperPASS, a New Aeroassist Tool," in *17th AIAA Aerodynamic Decelerator Systems Technology Conference and Seminar*, Monterey, 2003.

[5] J. L. Elliot, E. W. Dunham, A. S. Bosh, S. M. Slivan, L. A. Young, L. H. Wasserman and R. L. Millis, "Pluto's atmosphere," *Icarus,* vol. 77, pp. 148-170, 1989.

[6] W. B. Hubbard, D. M. Hunten, S. W. Dieters, K. M. Hill and R. D. Watson, "Occultation Evidence for an atmosphere of Pluto," *Nature,* vol. 336, pp. 452-454, 1988.

[7] R. L. Millis, L. H. Wasserman, O. G. Franz, R. A. Nye, J. L. Elliot, E. W. Dunham, A. S. Bosh, L. Young, S. Slivan and A. Gilmore, "Pluto's Radius and Atmosphere - Results from the entire 9 June 1988 Occulation Data Set," *Icarus,* vol. 105, p. 282, 1993.

[8] B. Sicardy, "Pluto's Atmosphere from the 2015 June 29 Ground-Based Stellar Occulation at the Time of New Horizons Flyby," *The Astrophysical Journal Letters,* vol. 812, no. 2, 2016.

[9] E. H. Dowell, Aeroelasticity of Plates and Shells, Leyden: Noordhoff International, 1975.

[10] B. D. Goldman, E. H. Dowell and R. C. Scott, "Flutter Analysis of the Thermal Protection Layer on the NASA HIAD," Daytona Beach, FL, 2013.

[11] B. D. Goldman, E. H. Dowell and R. C. Scott, "In-Flight Aeroelastic Stability of the Thermal Protection System on the NASA HIAD, Part II: Nonlinear Theory and Extended Aerodynamics," in *AIAA SciTech 2015*, Kissimmee, FL, 2015a.

[12] M. Tauber and K. Sutton, "Stagnation Point Radiative Heating Relations for Earth and Mars Entries," *Journal of Spacecraft,* vol. 28, no. 1, pp. 40-42, 1991.

[13] F. M. Cheatwood and P. A. Gnoffo, "User's Manual for the Langley Aerothermodynamic Upwind Relaxation Algorithm (LAURA)," NASA , Hampton, VA, 1996.

[14] C. I. o. T. Yuri Feldman, I. I. o. S. Arnab Samanta, C. I. o. T. Tim Colonius, J. P. F. M. Pauken, J. Hall, T. Colonius, M. Pauken and J. Jones, "Numerical and Experimental Modeling of Natural Convection for a Cryogenic Prototype of a Titan Montgolfiere," in *11th AIAA Aviation Technology, Integration, and Operations (ATIO) Conference*, Virginia Beach, VA, 2011.

[15] L. Carlson and W. Horn, "New Thermal and Trajectory Model for High Altitude Balloons," *Journal of Aircraft,* vol. 20, no. 6, pp. 500-507, 1983.

[16] L.Rubin and J.Larouco, "High Performance Balloon Envelope Materials for Planetary Aerobots," Foster Miller, MA, 2002.

[17] S. Heltzel and C. Semprimoschnig, "A Detailed Study on the Thermal Endurance of Kapton HN and Uplilex S," in *Proceedings of the 9th International Symposium on Materials in a Space Environment*, Noordwijk, The Netherlands, 2003.

[18] DuPont, "Dupont Kapton Summary of Properties," DuPont, 2017.

[19] Sheldahl, "thermal Control Overview," Sheldahl, Northfield, MN.

[20] A. S. Clair, W. Slemp and T. S. Clair, "High-Temperature Adhesives for Bonding Polyimide Film," 1980.

[21] Toyobo Co., Ltd., "PBO Fiber Zylon, Technical Information," Toyobo Co., Ltd., Kita-Ku, OSAKA, JP, 2005.

[22] E. Orndoff, "Development and Evaluation of Polybenzoxazole Fibrous Structures," 1995.

[23] S. Bourbigot and X. Flambard, "Heat Resistance and Flammability of High Performance Fibres: A Review," *Fire and Materials,* vol. 26, pp. 155-168, 2002.